Project Report
DLR-LA-RAK-VDY-RP-005

Applicability of radiation modeling for direct comparison of simulations and experiment

José Felix Zapata Usandivaras

Federica Tonti
Justin Hardi, PhD
11th September, 2020

DLR **Deutsches Zentrum für Luft- und Raumfahrt**
German Aerospace Center

Contents

Nomenclature

γ	Gas specific heat ratio
c^*	Characteristic velocity
c_f	Thrust coefficient
CH_4	Methane
g_0	Gravity constant
$I_{sp,vac}$	Specific impulse in vacuum
P_{cc}	Combustion chamber pressure
R	Ideal gas constant
T_c	Temperature of combustion
VR	Velocity ratio
CFD	Computational Fluid Dynamics
CP	Critical Point
DMD	Dynamic Mode Decomposition
LES	Large Eddy Simulation
LOX	Liquid Oxygen
LRE	Liquid Rocket Engine

OOP Object Oriented Programming

RTE Radiative Transfer Equation

UV Ultraviolet

List of Figures

List of Tables

1. Summary

In this report, the theoretical background and legacy work of the flame radiation simulation study performed by the *Combustion Dynamics* research group at DLR's *Institute for Space Propulsion* is presented. The work performed in the context of this project has been the enhancement of the already existing "Spectral Modeling and Ray Tracing" tool (SMART). The tool performs post-processing of CFD solutions with the goal of obtaining pseudo-radiation images for comparisons with experimental measurements. This project is framed within the team's plan to deepen their simulation capabilities to enrich the extensive experimental knowledge it holds in the domain of liquid rocket combustion.

A system engineering approach with requirements identification was taken to comply with the original work plan and deliverables lead-time. Thereby, the redesign and re-implementation of the original scripts inherited was done with an object-oriented approach; while taking special care at the segregation and single-responsibility principles at the moment of sketching the architecture.

The tool was applied on two test cases. On the first one, a benchmarking case, it was found that comparatively the tool predicts a smaller flame volume than original results. Origins of the differences are discussed though they represent the subject of future studies. On the second application case, an unsteady simulation of hydrogen-oxygen combustion, it was found that refraction in the wake of the LOX jet may influence significantly the frequency composition of the estimated radiation flux.

2. Introduction

In the realm of liquid rocket engines (LRE), study of the high frequency combustion instabilities that occur within these have been a major conundrum in their design. The phenomenon by which pressure oscillations interact with heat release fluctuations as a product of an unsteady combustion can lead to catastrophic failure of the engine, and thus likely that of the mission. Therefore, in the research context it is of paramount importance to understand the physics underlying this mechanism.

Up until recent, development of LREs was heavily dependent on testing, therefore the stability during operation of the engine being mostly derived from these. However, it has been due to the development of high-fidelity CFD simulations of combustion such as RANS, URANS, LES, DNS that this process has been simplified, to a given extent. However, simulation tools have to be validated against experimental data in order to assess their reliability. In particular, it is of interest for researchers to study the field distribution of several quantities such as pressure, temperature and heat release rate which cannot be measured experimentally, either due to the extreme conditions that are encountered inside a LRE or due to its very same nature. Among these variables, a key physical parameter is the heat release rate ($\dot{q}$).

On the other hand, a physical quantity which can be easily identified and measured is the OH* radiation, which can be quantified by high-speed imaging experimentally. OH* radiation is considered as a marker of the flame emission zone. In such context, one experimental technique commonly used is the high-speed imaging of flame radiation as it can be linked to the presence of emitting hydroxyl excited radicals (OH*).

The present project is intimately related to this technique. The focus has been laid on the redefinition, expansion and applicability study of the existing "Spectral Modeling and Ray-Tracing" tool (SMART) developed by Perovsěk and Tonti[10] for the radiation modeling of excited hydroxyl radicals. The final goal is to validate the visualization tool, which produces pseudo-radiation images of emitting OH* molecules from CFD simulation results, against the experimental data given by the high speed cameras. The visualization of the OH* molecules within the flame zone is given by the post-processing of the results produced by the numerical simulations of experimental rocket combustors.

The work performed within the frame of this project, and therefore the layout of the current report, has been divided into three main areas:

- Literature review
- Legacy software study, requirements identification and tool expansion, enhancement
- Tool assessment

2.1. Company Presentation

This project has been carried out within the *German Aerospace Center (DLR), Institute for Space Propulsion* in Lampoldshausen, Germany. The department responsible for hosting and supervising the project was the *Combustion Dynamics* research group, *Instabilities* team; nested inside the *Cryogenic Rocket Propulsion Department*. The organizational structure of the latter is shown in Figure 2.1.

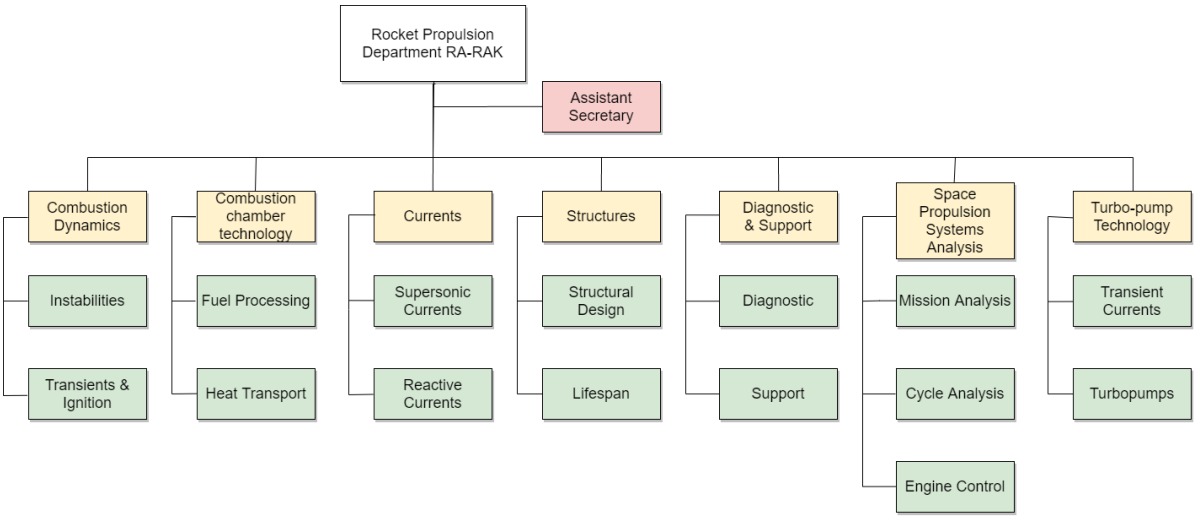

Figure 2.1.: **Organizational structure of the *Rocket Propulsion Department*.**

As a research group, its goal is to investigate, understand and predict combustion instabilities in liquid rocket engines thrust chambers. The group has access to a series of experimental rocket combustors. Coupled with a strong experimental approach, numerical simulations are conducted and are part of the group's expertise. Additionally, collaborations with external partners are conducted (*EM2C*, *IMFT*, among others).

Regarding the work dynamics, the team is made up of research associates hired full-time by the institute which are also in condition of Ph.D. students. Mentoring of interns and bachelor theses' students is performed by these.

It must be remarked that the *CoVid-19* crisis forced the work to be performed from home, thus hindering the communication flow typically found in an office. Nonetheless, due to the

nature of the present project, such hurdles were promptly solved once access to the company's computational resources was granted. The entirety of this project was done under the so called "home office" condition.

2.2. Scientific Background

The physics associated to the work done during this project is of multidisciplinary character as it involves the study of radiation and its modeling as a consequence of the combustion process taking place within LREs. The task in the current project has been primarily to expand and study the applicability of the SMART tool developed by Perovsĕk in [10]. However, it is necessary to first understand the scientific background that lies behind. Therefore, the following breakdown has been proposed: liquid engine combustion, radiation modeling and geometric optics.

2.2.1. Liquid Rocket Combustion

Liquid Rocket Engines are a breed of the chemical propulsion family in which an oxidant and a fuel, both stored in liquid phase, are mixed and ignited in a combustion chamber. The reaction, of exothermic character, increases the enthalpy of the flow. The energy release is converted into thrust by means of a nozzle which accelerates the flow.

Several examples are available, such as the $O_2 - H_2$ *Vulcan* engine or the $O_2 - CH_4$ *Prometheus* under development. In the context of this project, the focus has been laid on examples of hydrogen-oxygen combustion ($O_2 - H_2$).

2.2.1.1. Hydrogen-Oxygen Combustion in LREs

Liquid Hydrogen and Oxygen have been used persistently as a fuel-oxidant couple in the development of first stage and vacuum engines. The reason for this choice lies on the high temperature of combustion (T_c) as well as the relatively low molar mass (M) of the combustion products in comparison to other reactions products (such as the case of $O_2 - CH_4$ combustion). These properties translate into a high characteristic velocity(c^*) (see Eqn. 2.1) and consequently a high specific impulse in vacuum ($I_{sp,vac}$) . In Eqn. (2.1), γ, R, g_0, c_f refer to the specific-heat ratio of the combustion gases, the universal gas constant, gravity acceleration

and thrust coefficient, respectively.

$$\begin{cases} c^* = \left(\frac{\gamma+1}{2}\right)^{\frac{\gamma+1}{2(\gamma-1)}} \sqrt{\frac{RT_c}{\gamma M}} \\ I_{sp,vac} = \frac{c_f c^*}{g_0} \end{cases} \tag{2.1}$$

Furthermore, the propellants are non-premixed, which means that the mixing process and later combustion takes place exclusively within the combustion chamber. Hydrogen is typically injected in gaseous form whereas oxygen can be both injected in subcritical or supercritical conditions. These refer to the thermodynamic state of the fluid with respect to the critical point, identified by the critical pressure (p_{cr}) and temperature (T_{cr}), as shown in the the pressure-temperature diagram of Figure 2.2. Table 2.1 summarizes the critical properties for both fluids. Figure 2.3 sketches the injection jets in both situations.

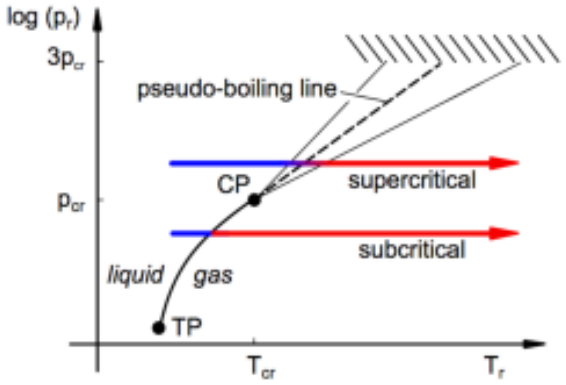

Figure 2.2.: **Pressure-temperature diagram displays the difference between subcritical and supercritical states. [10].**

Table 2.1.: **Critical properties for hydrogen and oxygen.[10].**

Property		H_2	O_2
Critical temperature	T_{cr} $[K]$	33.19	154.58
Critical pressure	p_{cr} $[MPa]$	1.313	5.043

Figure 2.3 provides better insight on the early mechanisms which dominate the mixing of fuel and oxidizer downstream of the injector plane. Sub-critical injection is characterized by the breakdown of the LOX core into smaller liquid droplets which later evaporate and mix with the hydrogen in gaseous phase an react. Even though mass transfer from the LOX core occurs in the form of diffusion as well as early evaporation, the dominant mechanism is the droplet formation or atomization. This is driven by the shear forces between both fluids which lead to the LOX jet desintegration and consequently greatly impacts the overall performance [13].

Supercritical oxygen injection in turn, does not generate droplets given the fact that there is no distinction in supercritical condition between a gas and a liquid phase and thus, surface tension goes to zero. Therefore, the mixing mechanism is commanded by the turbulent diffusion and the shear forces which break apart the LOX jet into smaller lumps.

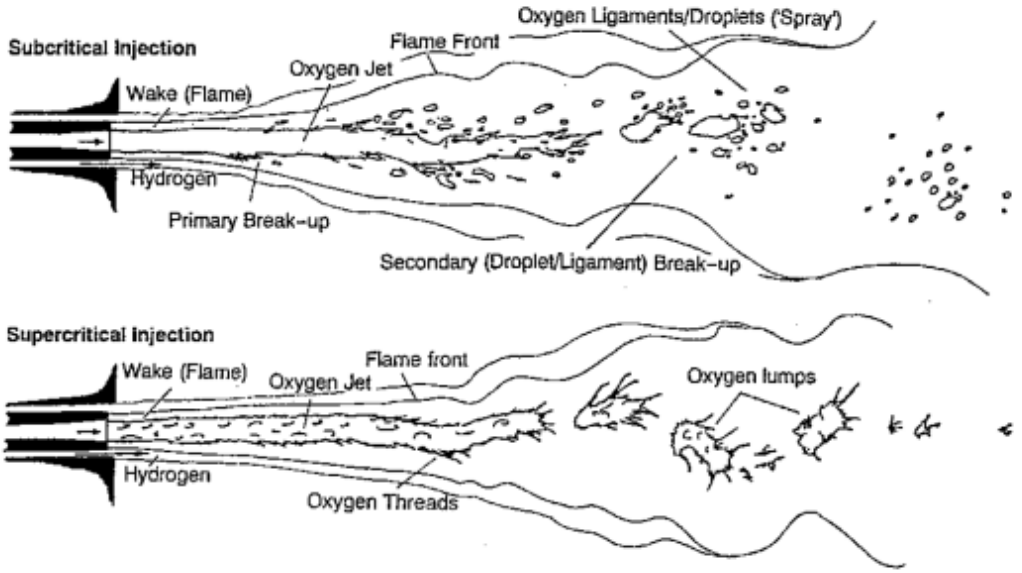

Figure 2.3.: **Schematics of a co-axial axisymmetric injector with gaseous hydrogen from the annulus and oxygen flowing through the center in both liquid and supercritical conditions. The LOX post has been recessed. [7].**

A key set of dimensionless numbers used to characterize this phenomenon are the velocity ratio (VR) and the momentum flux ratio (J) defined in Eqn. (2.2)[6].

$$VR = \frac{v_g}{v_l} \quad J = \frac{(\rho \cdot v^2)_g}{(\rho \cdot v^2)_l} \tag{2.2}$$

The global chemical reaction involving hydrogen and oxygen in LREs is,

$$2H_2 + O_2 \longrightarrow 2H_2O \tag{2.3}$$

2.2.1.2. Liquid Rocket Combustion Instability

Another important aspect related to LREs and their study is the understanding of the instabilities that may develop during operation. Although a proper description of the topic is out

of the scope of this work, it is important for the reader to familiarize with some basic concepts before proceeding with this document.

Combustion instability refers to mutually reinforced fluctuations in combustion energy release and combustion chamber pressure [15]. High-frequency components are those which oscillate with the frequency of the acoustic resonance of the thrust chamber volume. The origin of the excitation may come from any of the elementary processes of the combustion such as the injection, atomization, vaporisation or the chemical reaction dynamics. This phenomenon can result in catastrophic failure due to the large amplitudes of the pressure oscillations that can arise from it (greater than 20% of the combustion chamber mean pressure P_{cc}). Examples of combustion instabilities leading to catastrophic failure are the *Viking* engine on *Ariane L02* flight and the *Aestus* engine on the *Ariane 5 L510* flight.

A necessary (though not sufficient) condition to trigger these instabilities is that heat release fluctuations be coupled with acoustical pressure fluctuations. This is summarized by the well-known *Rayleigh* criterion [15] (Eqn. 2.4).

$$\int \int_{V,t} p' \dot{q}' \, dt dV > 0 \tag{2.4}$$

In which $p = \overline{p} + p'$ represents the pressure field with p' and $\overline{p}$ being the fluctuating and steady components of it, respectively. Similarly this applies to the heat release rate per unit volume, $\dot{q}$.

With this in mind it is possible to understand the cumbersome nature of liquid rocket engines design when it comes to stability and robustness. Heat release rate is a magnitude at most times difficult to quantify nor impossible to measure experimentally. Thus, this leads to intensive testing as the method to study these phenomenons. Even though the availability of high-fidelity combustion modeling through CFD of combustion has provided insight on the matter, still validation of such codes through experimental data proves to be a perennial problem.

According to Fiala [3] in combustion instability research the local volumetric heat release it is often assumed by the measure of the emitted radiation from excited radicals, mostly OH* and CH* (due to their well defined spectra). Experimental combustors with optical access allow high-speed imaging of the flame in the desired wavelengths.

It was concluded by Fiala [10] in his work with laminar hydrogen-oxygen flames, that there is non evident spatial correlation between the local heat release and the OH* radiation. Nonetheless, the technique of excited radicals radiation photography can still be used as a means to contrast with pseudo-radiation imaging estimates obtained from the CFD solutions.

To achieve so, it is necessary to describe the available radiation models and how this information can be derived from the CFD solutions.

2.2.2. Flame Radiation Modeling

A typical example of flame radiation is the one observed in a light candle (Figure 2.4). In the visible range, blue radiation is detected at the center of the flame whereas in the rest only yellow is visible. The former is linked to the chemiluminescence of the excited methylidyne radical CH* and the latter to hot unburnt carbon particles product of incomplete combustion, termed soot [3]. In addition, the flame also emits in other frequency bands of the radiation spectrum other than the visible range, including UV and infrared ranges.

Figure 2.4.: **Close-up picture of a candle flame [3].**

As with the CH* chemiluminescence responsible for blue radiation in candles, hydrogen-oxygen combustion flames are characterized by the chemiluminescence and thermal excitation of the previously mentioned hydroxyl radical OH. In its excited state, OH*, this molecule has a distinctive transition with spectral emission signature in the UV region which makes it interesting for experimental purposes. As it has little overlap in the wavelengths of interest, with the emission of spectra of other emitting molecules and hardware[1] present in combustion chambers in LREs.

2.2.2.1. Origin of the OH* radical and reaction scheme

The main purpose of this work is to construct pseudo-images from the radiation of the excited hydroxyl molecule OH (OH*). For such it is necessary to understand the different mechanisms of molecule excitation. In summary, these are [3]:

1. Thermal collision with another molecule, and exciting the target molecule through trans-

[1] Emitting hardware present in combustion chambers associates to any surface in the combustion chamber. These are emit according to Planck's black-body, following emitted radiation intensity profile which is function of its temperature.

lational energy transfer:

$$M + Q \rightleftharpoons M^* + Q \tag{2.5}$$

2. Photonic absorption:

$$M + h\nu \rightleftharpoons M^* \tag{2.6}$$

3. Chemical reaction resulting on the excited species (chemiluminescence):

$$A + B \rightleftharpoons M^* \tag{2.7}$$

or considering a third molecule,

$$A + B + Q \rightleftharpoons M^* + Q \tag{2.8}$$

The last mechanism points to the chemical origin of the excited hydroxyl radicals. Radiation emission from these is named as chemiluminescence, as these are the result of a chemical reaction instead of a thermal collision. A complete description of the reactions that lead to the formation of OH and OH* molecules is thus given by,

$$\begin{array}{c} H_2 + O_2 \longrightarrow 2OH \\ H + O_2 \longrightarrow OH + O \\ O + H_2 \longrightarrow OH + H \\ O + H + M \longrightarrow OH^* + M \\ O_2 + H \longrightarrow OH^* + H_2O \end{array} \tag{2.9}$$

in which M corresponds to a third molecule. When doing numerical simulations of combustion, an advantage of this kinetic scheme is that it permits the appropriate modeling of the transport of OH* [3, 9], as the excited radical is treated as a separate species. However, this approach is computationally expensive as all of the possible molecules M have to be considered, hence adding to the total number of chemical reactions to consider in the kinetic scheme.

One important conclusion from Fiala [3] though is: "The presence of excited OH* molecules in flames typical for liquid rocket combustion is mostly due to thermal excitation. Chemical excitation, which is the origin of chemiluminescence in colder flames, is generally negligible".

By neglecting the chemical origin of the excited species OH*, the reaction scheme shown in Eqn. (2.9) is reduced to:

$$\begin{aligned} H_2 + O_2 &\longrightarrow 2OH \\ H + O_2 &\longrightarrow OH + O \\ O + H_2 &\longrightarrow OH + H \end{aligned} \tag{2.10}$$

Compared to the set of equations in Eqn. (2.9), the latter is considerably less expensive in terms of computational costs as the set of reactions $O + H + M \longrightarrow OH^* + M$ is not considered. The simplified approach considers only 6 molecules (H_2O, H_2, O_2, OH, H and O) and 7 reactions (including those were OH is not present). This scheme was used by Beinke [2] in the simulations of DLRs *BKH* experimental combustor, over which the first analysis of SMART was done.

Finally, it is worth mentioning that in flames with temperatures above 2700 K the populations of OH and OH* are in thermal equilibrium. In such case both are related through Boltzmann's distribution (Eqn. 2.11) where $\Delta_{OH^* \rightarrow OH} g_m^0$ is the difference of standard molar free Gibbs energy between the excited and ground state species and R_m the gas constant. $[OH^*]$ and $[OH]$ refer to the concentrations of the OH* and OH species, respectively.

$$\frac{[OH^*]}{[OH]} = \exp\left(-\frac{\Delta_{OH^* \rightarrow OH} g_m^0}{R_m T}\right) \tag{2.11}$$

2.2.2.2. OH* emission spectra

Electromagnetic radiation may be modeled as waves of coupled electric and magnetic fields traveling through space, or as packets of discrete energy (ΔE) called photos whose energy is linked to their frequency (f) by Eqn. (2.12), where h represents Planck's constant.

$$\Delta E = hf \tag{2.12}$$

It is known that within a single atom, electrons are allocated following well defined energy levels, characterized by a set of quantum numbers. Electronic transition between energy levels results in the emission or absorption of a photon whose wavelength is determined by Eqn. (2.12). Discrete combinations of the transitions of the electrons in an atom from an excited state[2] to its ground state[3] provide then the location of the spectral lines which characterize the atom.

[2] Electron allotted into a greater energy level, due to interaction with another particle.

[3] Non-excited energy level of the electron obtained from solving the eigenvalues of the *Hamiltonian* operator in *Schrodinger's* time-independent equation.

When it comes to molecules, compared to atoms, its multi-atomic nature implies that it is not only electronic transition which determines photonic emission and absorption, but also energy transitions in its constituents relative vibration and rotation. The energy associated to these is also quantized.

The population of posible transitions between energy levels at a given excited molecule is enlarged as electronic, rotational and vibrational transitions may occur simultaneously. Electronic transition governs the frequencies of them and this may be seen on the resulting spectra as smaller spikes located in vicinity of the main electronic transition peaks.

The strengths of the lines in the resulting spectra will be determined by the probability of the transitions associated to their frequencies. The transition probability is described by *Einstein* coefficients[4] and these are independent of temperature and pressure.

Even though transitions are associated to photons of a specific frequency and it would be expected that this yields a discrete spectrum, a phenomenon termed as *line broadening* explains the existence of rather intensity profiles linked to these transitions instead of lines. This is a consequence of multiple mechanisms, namely Doppler effect, Heisenberg's uncertainty principle in time-evolving systems (also called life-time broadening) and collisional broadening. These are dependent on pressure and temperature.

For the OH* emission-absorption spectra, there may be multiple transitions. It is of interest to this project the system of transitions between the excited $A^2\Gamma^+$ and the $\chi^2\Pi_i$ ground state [10]. For such system of transitions, the calculated spectra is given in Figure 2.5. The strongest emission and absorption is observed in the $307 - 320\ nm$ band.

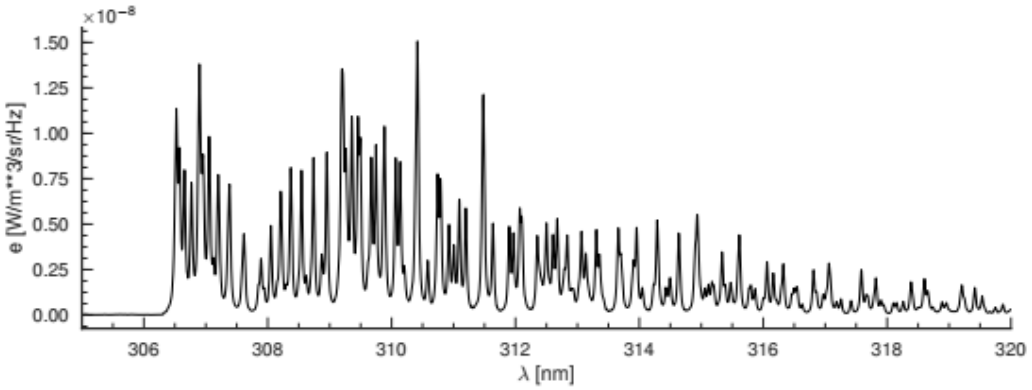

Figure 2.5.: OH^* **emission spectrum at** 62 bar, 3000 K **and** 0.15 **OH mass fraction. [10].**

[4] $A_{M' \to M''}$ is the transition probability for spontaneous photonic emission between the electronic excited state M' and its ground state M''.

2.2.2.3. Radiation Transfer

The problem of radiation transfer is mathematically described by the Radiative Transfer Equation (RTE) [14]. This equation (2.13), describes the change of the radiative intensity along a ray by performing the energy balance on the radiative energy travelling in a given direction $\vec{u}$ between locations s and $s + ds$.

$$\frac{1}{c}\frac{\partial I_\nu(s,\vec{u})}{\partial t} + \frac{\partial I_\nu(s,\vec{u})}{\partial s} = \eta_\nu(s) + \frac{\sigma_\nu(s)}{4\pi}\int_{4\pi} I_\nu(s,\vec{u}')\phi_\nu(s,\vec{u}' \rightarrow \vec{u})d\Omega' - (\kappa_\nu(s) + \sigma_\nu(s))\, I_\nu(s,\vec{u}) \tag{2.13}$$

The magnitude of interest is the directional radiation intensity ($I_\nu(s,\vec{u})$) defined as the radiative energy flow per unit time (t), unit solid angle (Ω), unit wavenumber (ν) and unit area normal to the considered direction ($\vec{u}$). All the coefficients, emission (η_ν), absorption (κ_ν) and scattering (σ_ν) are wavenumber dependent and considered isotropic.

It is worth to explain the terms of the equation in detail to clarify their physical meaning:

- $\frac{1}{c}\frac{\partial I_\nu(s,\vec{u})}{\partial t}$: the transient term. For the purposes of this project it is considered negligible as the electromagnetic radiation propagation (c) within the combustion chamber walls is considered instantaneous compared to the related fluid flow.

- $\frac{\partial I_\nu(s,\vec{u})}{\partial s}$: partial derivative of the radiation intensity along the ray with respect to the ray coordinate.

- $\eta_\nu(s)$: emission term, it is considered as a source of radiation intensity per wavenumber.

- $\frac{\sigma_\nu(s)}{4\pi}\int_{4\pi} I_\nu(s,\vec{u}')\phi_\nu(s,\vec{u}' \rightarrow \vec{u})d\Omega'$: incoming scattering term. Scattering is a phenomenon that occurs when incoming photons interact with particles of matter and exchange momentum or energy and thus are deflected from their original direction of propagation and may also result in change of wavelength (inelastic scattering) or not (elastic scattering) depending on the collision. The integral is performed over the entire solid angle domain (4π) as all possible directions have to be accounted for. This phenomenon is neglected as it is the case for molecular gases [3, 8].

- $\kappa_\nu(s)I_\nu(s,\vec{u})$: absorption. When considering an optically thin medium this term might be neglected. However, as concluded by Fiala [3], this is not applicable when modeling the OH* radiation, as self-absorption from OH molecules in the combustion chamber plays a significant role.

- $\sigma_\nu(s)I_\nu(s,\vec{u})$: losses due to scattering. Similar to incoming scattering, this term is neglected for molecular gasses.

Neglecting the aforementioned terms, Eqn. (2.13) reduces to,

$$\frac{\partial I_\nu(s,\vec{u})}{\partial s} = \eta_\nu(s) - \kappa_\nu(s) I_\nu(s,\vec{u}) \tag{2.14}$$

Eqn. (2.14) is a first order implicit equation which may be numerically solved by using a *Runge-Kutta* method by integrating from the initial ray coordinate (s_{B_0}: combustion chamber wall) to a given point in the medium s as it is done in the implementation of the SMART tool.

The initial condition for the differential Eqn. (2.14), is given by the directed radiation intensity at the boundary, $I_\nu(s_{B_0},\vec{u})$. In the context of this project, combustion chamber walls are modeled as black-bodies with a given emissivity and reflectivity. In the temperatures involved in LREs, black-body radiation emission in the spectral range which concerns OH* (mainly UV) is considered negligible as most of the radiation is emitted in the infrared range. As for the reflection in this region of the spectrum, walls are taken to be opaque surfaces [10].

Then, if the focus is only laid on the wavenumbers which involve OH* radiation, the initial value of the solution, which corresponds to the radiation emitted and reflected by the wall in these wavenumbers is then $I_{\nu,OH^*(s_{B_0},\vec{u})} \approx 0$.

2.2.3. Geometric Optics

As already described in the previous section, Eqn. (2.13) describes the radiative energy balance done along a *ray* segment with direction $\vec{u}$. However, it is necessary to introduce the concept of *ray*.

A ray is a construct used in geometric optics to interpret the path of electromagnetic radiation. It is known, from Maxwell's equations, that electromagnetic radiation energy propagates through space in the form of three-dimensional waves. A ray is then the curve defined by a point in the wavefront with tangent vector equivalent to the normal direction to the wavefront at that point.

As the radiation travels through a medium which is not vacuum, it undergoes a change in the speed of propagation (c) defined by the local magnetic and electric permeability (μ,ϵ). The ratio of the speed in vacuum (c_0) to the local speed in the medium is known as refraction index and is dependent on the wavelength of the radiation.

$$n(\lambda) = \frac{c_0}{c} \tag{2.15}$$

Gradients or changes in the refraction index of the media induce changes in the direction of the rays, a phenomenon termed refraction. In continuum media with refraction index gradients, the path followed by the rays is synthesized by the *Eikonal* equation. (Eqn. 2.16).

$$\frac{d}{ds}\left(n(\boldsymbol{r})\frac{d\boldsymbol{r}}{ds}\right) = \vec{\nabla}n(\boldsymbol{r}) \tag{2.16}$$

with s being the length along the curve of the ray. Introducing the variable $\boldsymbol{T}(s) = n(\boldsymbol{r})\frac{d\boldsymbol{r}}{ds}$, the equation may be reframed as a multidimensional implicit equation of the form $\frac{d\boldsymbol{X}}{ds} = \boldsymbol{F}(\boldsymbol{X}, \frac{d\boldsymbol{X}}{ds})$ as shown in Eqn. (2.17).

$$\frac{d}{ds}\begin{bmatrix}\boldsymbol{r}\\ \boldsymbol{T}\end{bmatrix}(s) = \begin{bmatrix}\frac{\boldsymbol{T}(s)}{n(\boldsymbol{r})}\\ \vec{\nabla}(\boldsymbol{r})\end{bmatrix} \tag{2.17}$$

This system may be solved numerically with a *Runge-Kutta* method and providing the initial values of the variables involved, namely: $\boldsymbol{T}(s_0) = n(\boldsymbol{r}(s_0))\frac{d\boldsymbol{r}}{ds}(s_0)$ and $\boldsymbol{r}(s_0)$.

The validity of the *Eikonal* equation is limited to C^1 refraction index fields. In C^0 domains the treatment of refraction index field discontinuities may be done by means of the *Snell's* law (Eqn. 2.18).

$$n_{\partial\Omega^+}\sin(\hat{d}_{\partial\Omega^+}, \hat{n}_{\partial\Omega^+}) = n_{\partial\Omega^-}\sin(\hat{d}_{\partial\Omega^-}, \hat{n}_{\partial\Omega^-}) \tag{2.18}$$

in which $\hat{d}$ and $\hat{n}$ denote the ray director and normal unit vectors in the vicinity of the interface $\partial\Omega$ in both the incident side $(+)$ and the departing side $(-)$.

2.2.3.1. Gladstone-Dale Equation

In the present section, the details of the refraction index field determination as derived in [10] will be briefly explained. For continuum media with density gradients originating from pressure, temperature or composition gradients the refraction index ($n(\boldsymbol{r})$) is modeled by the *Gladstone-Dale* equation (Eqn. 2.19).

$$n(\lambda, p, T, x_i) = 1 + \rho(p, T, x_i)\sum_{i=0}^{n} k(\lambda)_i x_i \tag{2.19}$$

where p, T, ρ and x_i correspond to the local pressure, temperature, density and molar fraction of component i of the mixture. k_i is the *Gladstone-Dale* coefficient for the species i, independent

of pressure and temperature. As expected, the refraction-index is dependent on the radiation wavelength (λ) and so are the coefficients.

Replacing the molar fractions by the mass fractions of components, and defining a wavelength of reference[5] the refraction index field is given by:

$$n_{\lambda_{ref}}(\boldsymbol{r}) = 1 + \rho(\boldsymbol{r}) \frac{\sum_{i=0}^{n} k_{\lambda_{ref},i} w_i(\boldsymbol{r})/M_i}{\sum_{i=0}^{n} w_i(\boldsymbol{r})/M_i} \tag{2.20}$$

It is important to remark that Eqn. (2.20) is valid to the extent to which the combustion chamber media is C^1. This is affected by the injection conditions of oxygen. In supercritical states, there is no actual difference between the liquid and gas, driving surface tension to zero. Consequently, no phase interfaces develop and the media is optically continuous. In sub-critical states, this does not hold as gas-liquid interfaces appear and refraction at these is commanded by *Snell's* law.

[5] OH^* radiation is studied over a limited section of the spectrum, the $[305 - 320]$ nm range. Perovsěk [10] concluded that dispersion in the refractive index was less than 1% for different wavelengths in the range of interest. Therefore, the refraction index is calculated for a central wavelength of $\lambda_{ref} = 312.5$ nm.

2.3. Objectives

The objectives defined by the *Combustion Instabilities* team for this project are divided in the following tasks:

1. Review of the literature to understand non-premixed liquid rocket combustion, the phenomenon of flame radiation and the associated models to it. Study the pseudo-radiation imaging technique and its use in experiments with research rocket combustors.

2. Review of DLR available spectral modeling scripts:

   Among the existing spectral modeling programs in DLR, there are the ones developed by Perovsěk [10] and Fiala [3] for specific applications and combustor setups. The current project focuses in the former, further explained in Section 3.1.

   Consisting of a single script written in *Python* in a procedural paradigm and tailored to visualize the OH* radiation in a specific combustor geometry; the task consists in studying the algorithm's lower level breakdown.

3. Reconfiguration and application of SMART tool to other CFD hydrogen-oxygen combustion simulations and analysis of results. Cases to consider in order of importance:

   a Laminar flame simulations:

   The objective is to use the steady-state laminar flame simulations performed by Fiala [3] in *Fluent* and post-process them via the SMART tool to obtain a visualization of the OH* radiation. Comparison of the images yielded by the tool and codes developed by Fiala [3] is expected. Account for the geometry of the combustor (cylindrical) and access windows must be done to accurately determine the rays trajectory.

   b REST HF-9 quasi-1D dynamic test case

   Apply the SMART tool over hydrogen-oxygen combustion URANS simulations carried out by Tonti on a single injector belonging to the 42-injector *BKD* experimental combustor. The flow is subjected to an external excitation pressure with frequency equal to that of the first-transversal mode (1T) of the chamber.

   The objective is to model the collected OH* radiation flux collected by an optical probe located at the measurement ring of the combustor. An analysis of the transient signal is expected.

   The combustor and nested CFD domain boundary geometries (cylindrical) must be

accounted for as well as the internal geometry of the optical probe.

4. SMART performance improvement

   The parallelisation of the code through the *Python* "multiprocessing" library is proposed.

In essence, the core of the work plan lies around expanding the algorithm developed by Perovsěk [10] and applying it to post-process CFD simulations of rocket combustors used at DLR.

3. Methodology

3.1. Pre-existing algorithm

The original algorithm underlying the "Spectral Modeling and Ray Tracing" tool (SMART) was developed by Perovsěk in [10]. It was conceived as a post-processing tool of 3D CFD solutions of combustion on a domain with rectangular cross-section and flat optical access windows. No refraction was accounted for at the window and rays incidence was considered parallel to it. The goal of the algorithm was to generate OH* pseudo-radiation images comparable to those collected by the high-speed cameras in the experimental setup of *DLR BKH* research combustor (see Figure 3.1).

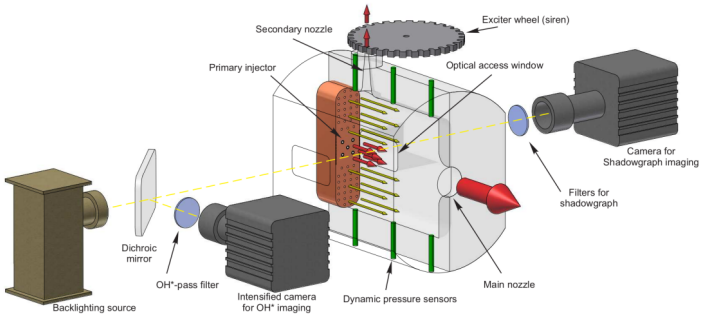

Figure 3.1.: ***BKH* experimental setup schematics. [10]**

The steps which define the algorithm are summarized below and illustrated on Figure 3.2.

1. *Load data*: the data from the CFD simulations of the hydrogen-oxygen combustion of interest is loaded in memory and cropped, if necessary. This includes both results data as well as grid data.

2. *Define pixels of the results image*: The rays over which OH^* radiation is determined are linked to each of the pixels of the camera in a matrix array.

3. *Calculate the ray path for the pixel*: starting by one ray, its path along the combustion chamber is determined by means of the method described to solve the *Eikonal* equation (Section 2.2.3). The starting point of the ray is the inner surface of the flat window. The

starting direction is taken as normal to the plane of the window (z direction in Figure 3.2).

4. *Simulate the OH^* spectra for the points on the ray*: the spectral simulation is performed for every point the ray by specifying pressure, temperature and mass fractions of the species (in ground state) at the point of interest. The simulation is performed by a wrapped C based library developed during the *DLR TAU* project enabled to work on *Python*. The simulation yields the coefficients κ_ν and η_ν for the requested wave-numbers (defined by discretizing the range of wavelengths $[305 - 320]\ nm$).

5. *Multiply the spectral radiance with the spectral filter transmittance and integrate*: in the experimental setup, in order to be able to capture incoming radiation to the camera in the range of interest, a band-pass filter is set on top of the camera. The filtering is done by integrating the product of the filter transmittance ($\tau_{filt}(\nu)$) by the radiance at the exit of the combustion-chamber.

$$I_{filt}(\vec{u}) = \int_{\nu_1}^{\nu_2} I_\nu(s_f, \vec{u}) \tau_{filt}(\nu) d\nu,\ \tau_{filt}(\nu) \leq 1.0 \tag{3.1}$$

6. *Save the last radiance value to a 2D array*: algorithm data is stored for later display or further processing.

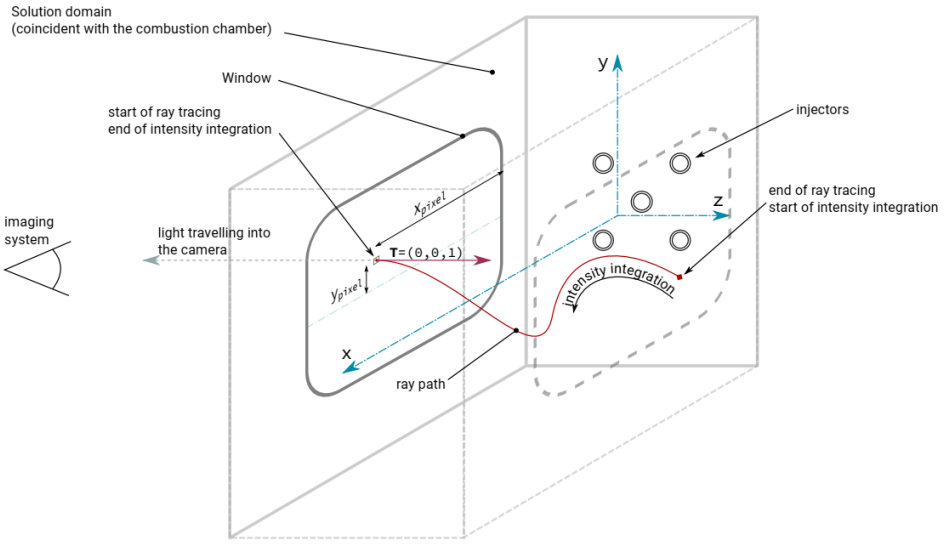

Figure 3.2.: **Ray tracing depiction and RTE integration. Image from [10].**

3.2. Requirements

Based on the objectives defined for the project in Section 2.3 and additional remarks discussed with the *Combustion Instabilities* team, a systems engineering approach was taken. The objectives revolve around expanding the SMART tool to different experimental rocket combustors with optical access.

First iteration of the tool consisted of a *Python* script tailored to operate with the configuration of a combustor with flat windows and rectangular cross-section domain with little to none reusability. Henceforth, it was deemed necessary to switch the work paradigm from script adaptation to that of developing a more comprehensive software that is general and flexible enough to account for the cases of interest. Additionally, due to the coronavirus crisis, access to the data from DLR was delayed, therefore a general approach which would tackle all the objectives at once was chosen. Even though more time-consuming, once solved it would yield a tool which would *a priori* satisfy the objectives defined.

The requirements identified from the objectives for such tool are listed in Table 3.1.

Table 3.1.: **Requirements identified for the desired computational tool.**

Description	**Tag**
The tool must model the OH^* radiation following the approach from [10]	MOD-1
The tool must be capable to model the behavior of multiple optical devices (camera, optical probe)	MOD-2
The tool must be capable to operate with different window and combustor geometries (flat, cylindrical, etc)	MOD-3
The tool must allow modeling of other combustion mixtures other than hydrogen-oxygen (original case for [10])	MOD-4
The tool must be capable of performing the ray-tracing in a three dimensional space	MOD-5
The tool has to be parallelizable	PER-1
The tool has to be capable of handling CFD solution data from different sources (*TAU*, *Fluent*, *ABVP*, etc)	FEAT-1
The tool must allow fast re-configuration (<1 week) from case to case	FEAT-2

In Table 3.1 tags *MOD*, *PER* and *FEAT* refer to modeling, performance and feature respectively.

In view of the requirements, it was decided that an Object Oriented Programming (OOP) approach was necessary to satisfy them in the development time allocated for this project. The main reason for this decision is based on two principles of OOP, abstraction and polymorphism. The former is useful when dealing with multiple cases but which can be nucleated under a single behavioral concept (for instance windows geometries, data sources, optical devices, etc), the latter refers to the idea that a single intent of behavior identified under the name of a method or

function may have different implementation depending on the commanding object (for instance, ray-tracing with a circular window differs from a planar window, a camera treatment from an optical probe, etc).

3.3. SMART proposed architecture overview

A simplified schema of the proposed architecture for SMART, intended to comply with the requirements listed before is shown in Figure 3.3. Class diagrams and further explanations on the new SMART architecture are provided on Appendix A.

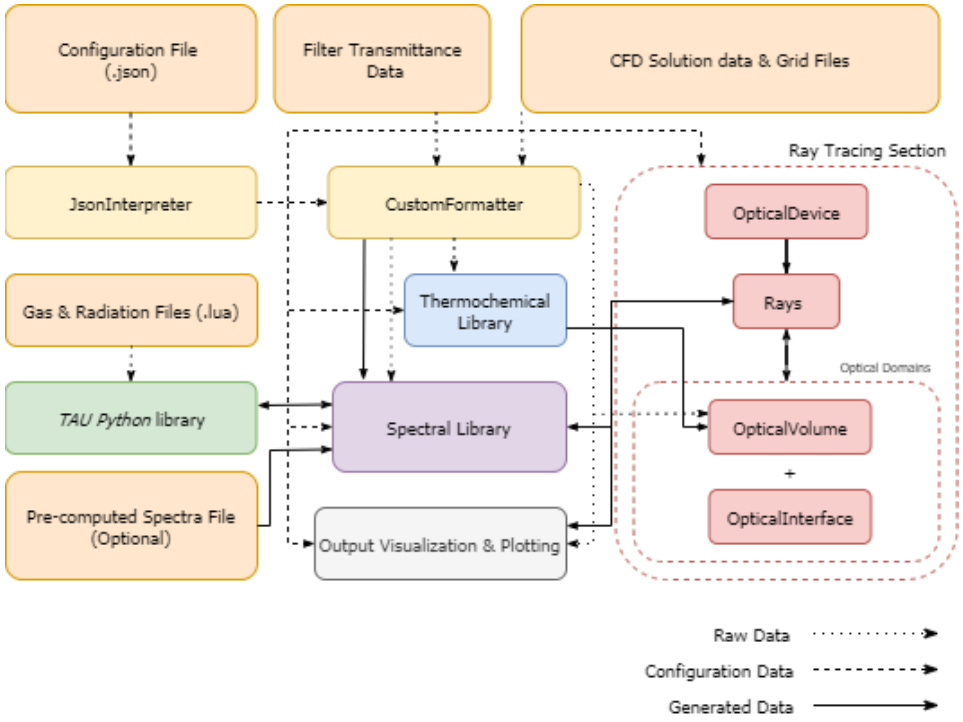

Figure 3.3.: **SMART proposed architecture schema.**

A description of the objects shown in Figure 3.3 is given below.

- *Data files* (Orange)

  1. *Configuration File*: The configuration file is a *.json* file which contains the data required for the initialization of the objects in memory. This information is uniquely linked to the case that is being simulated. Examples of such data include: species present and chemical constants; geometry of the combustor being studied and windows; camera location, pixels and pointing direction, and CFD and radiation files directories, among others.

2. *CFD Solution & grid data file*: includes the combustion CFD results as well as the corresponding grid of the CFD domain on which the post-processing is performed.

3. *Gas & radiation (.lua) files*: required to perform the spectral modeling as they serve as data-bases for the gas properties and spectral lines of the species present in the chamber.

4. *Filter transmittance data*: table which contains the camera filter transmittance ($\tau_{filt}(\nu)$) as a function of the radiation wavelength.

5. *Pre-computed Spectra file*: inherited from the algorithm of Perovsĕk [10]. It serves as a database for radiation quantities (κ_ν and η_ν). The objective of it is to optimize computing times. This is done through sampling of the radiation quantities at specific pre-defined points of operation and *a posteriori* interpolation. This file is not essential for the algorithm to run.

- *Data interfaces* (yellow):

1. *JsonInterpreter*: object designed to act as interface between the configuration file and possible configuration data clients.

2. *CustomFormatter*: object designed to interpret the CFD solution and & grid data. Is has the role of performing necessary operations and formatting on the CFD results, and in that way prepare them to be consumed by other sections of the software. Formatting operations may include: unit conversion, domain cropping, grid re-sampling. Additionally, it interprets the filter data from its file.

- *Ray tracing section* (red): This section is linked with all that concerns the inverse ray tracing. From their source point to their end-point in the combustion chamber wall. A detailed derivation of the ray tracing relations implemented in the algorithm can be found in Appendix B.

1. *OpticalDevices*: these objects are associated to optical instruments such as cameras or probes. Their main function is the definition of the *Rays* instances to be used in the inverse ray tracing, by specifying their origin point and direction.

2. *Rays*: this object is a representation in the software of the ray concept mentioned in the Section 2.2.3.

3. *OpticalInterface*: program representation of any two dimensional object which may alter the path of the ray. For example a refractive interface located at the combustor window.

4. *OpticalVolume*: this object is implemented to account for the refraction in the continuous media inside the combustion chamber. The rays are propagated through the

volume by integration of the *Eikonal* equation (2.16) and using the refraction index field from the *Thermochemical library*. Any grid data is provided by the *Custom-Formatter*.

- *Thermochemical library* (blue): collection of classes meant to be used to define the species present in the combustion mixture and serve as a host of relevant chemical data associated to these. It performs the calculation of the refraction index field via Eqn. (2.20). It provides the *Spectral library* with the mass fractions of the species.

- *Spectral library* (purple): section of the code in charge of determining the spectral quantities at the different ray path points. This is done by performing successive requests to the *TAU Python library* with local pressure, temperature and mass fractions of species. Later it integrates the RTE (Eqn. 2.14) along the ray path and performs the band-pass filtering based on the filter transmittance to obtain the estimated integrated radiance.

- *TAU Python library* (green): Includes *gaspy.py* and *radpy.py* files. These are *Python* wrapped *C* dependencies which calculate the spectral quantities by simulating the spectra of the requested molecule in the specified wavenumbers.

- *Output visualization & plotting* (gray): for generation of pseudo-radiation images or calculation of radiative flux, the information stored at the *Rays* instances is processed and prepared for display.

3.4. Development remarks

Further remarks have to be made regarding the code described above. These include:

1. The code was developed in *Python 2*. Although sunset in January 2020 and IT directives to migrate to *Python 3* within *DLR*, the chosen platform of development was *Python 2* as the *TAU Project Python* wrapped *C* libraries mentioned were compiled to only work in *Python 2* and migration to *Python 3* is not yet available. Nonetheless, for future uses, the entirety of the code was developed using the *Python* package **"six"** to safeguard cross-compatibility excepting external libraries.

2. The code relies heavily on the **"numpy"** and **"scipy"** libraries as these are optimized for numerical computation. To test the implementation of the ray propagation module the *Luneburg* lens case was implemented as it was used similarly as benchmark by Perovšek in [10]. A description of this case is shown in Appendix D.

4. Results

In the present section, the results yielded from the application of the redesigned SMART tool to specific cases is presented alongside the particularities associated to each of these.

4.1. Test case A: Fiala laminar flame

In his doctoral thesis titled *"Radiation from High Pressure Hydrogen-Oxygen Flames and its Use in Assessing Rocket Combustion Instability"* [3], Fiala proceeded to study the emission in hydrogen-oxygen flames. His work included not only the design and construction of a experimental combustor with optical access to study O_2-H_2 laminar-flames by performing high-speed photography of the OH* and blue radiation at different conditions, but also the CFD steady-state simulations in *Fluent* and OH* radiation pseudo-imaging through different models to assess the validity of certain hypotheses'.

In the present project, the Fiala cases are intended to be used as benchmark of the re-designed SMART tool.

4.1.1. Experimental setup

A schematic of the experimental combustor used is shown on Figure 4.1a. The system is formed by a quartz lance coaxial to a quartz shield. Oxygen flows through the lance whereas hydrogen flows through the annulus. Side quartz windows are in place at the expected flame location to capture radiation from the combustion by a camera aligned with them as portrayed in Figure 4.1b. Additional background illumination is provided as part of the experimental setup to improve the signal to noise ratio of the radiation measured by the camera.

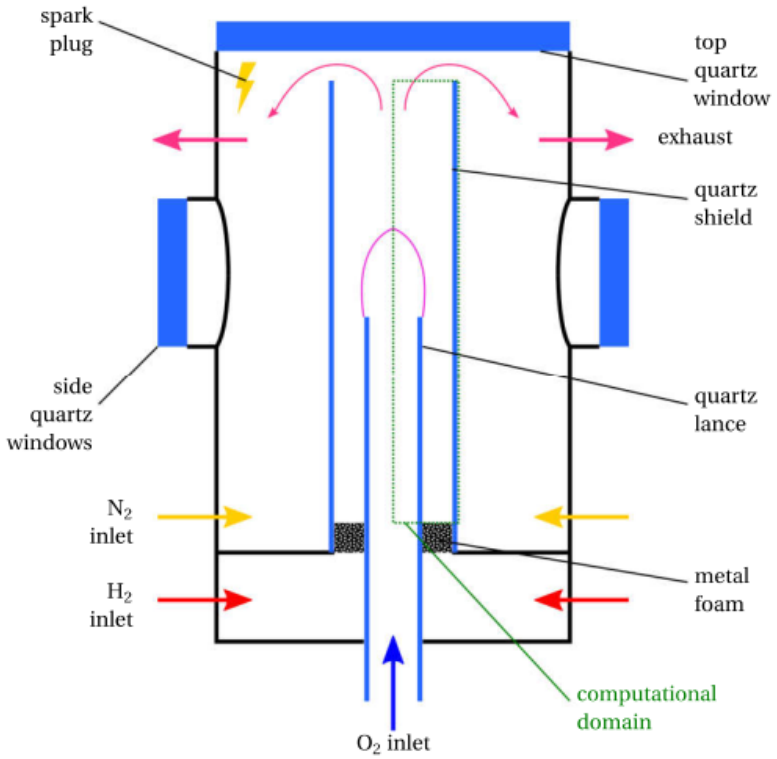

(a) Schematics of combustor used by Fiala.

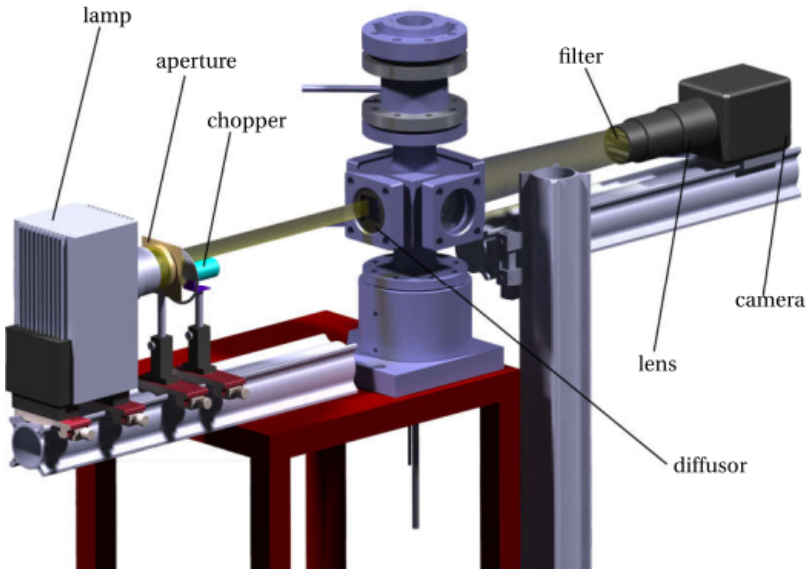

(b) Camera and background illumination setup used by Fiala.

Figure 4.1.: Experimental assembly used by Fiala [3].

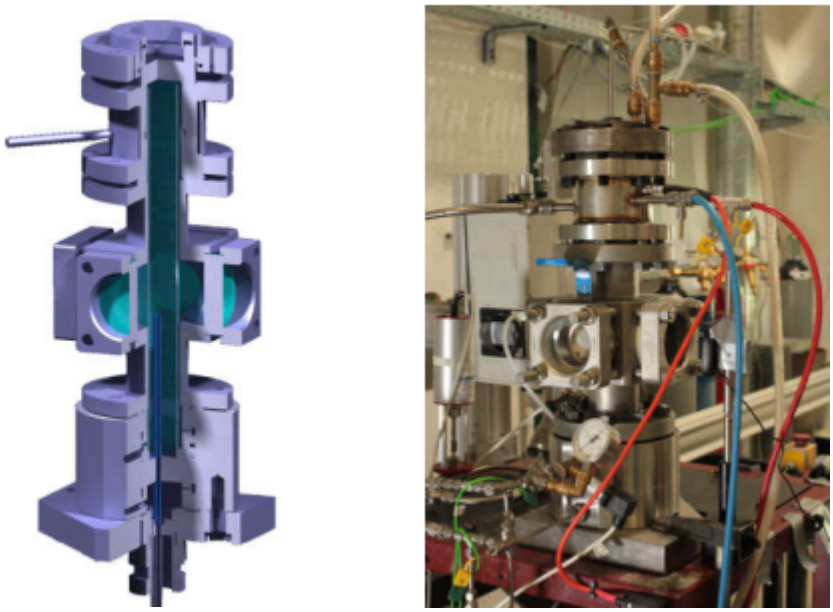

Figure 4.2.: **CAD and photography of final assembly of combustor used by Fiala [3].**

4.1.2. Fiala simulations

The CFD simulations carried out by Fiala were done in *Fluent* following the detailed kinetic schemes shown in Eqn. (2.9) treating the OH* as a separate species. The domain used is axisymmetric with and average cell size of 0.5 mm (Figure 4.3). The boundaries of the domain used have been sketched in green in Figure 4.2.

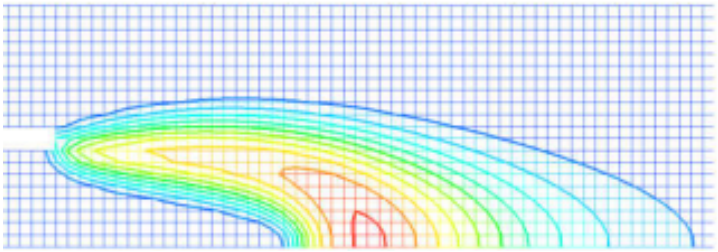

Figure 4.3.: *OH* **mass fraction contour overlaid on mesh used by Fiala [3].**

For the OH* pseudo-radiation imaging, a similar technique to that of ray-tracing was adopted. Rays were generated at the camera position from a unique point located in the injection plane (see Figure 4.4). Each ray was linked to a pixel. Later, the 2D ray arrangement is translated along the combustor axis to make the 3D rays matrix. Refraction at the quartz windows and shield was accounted for, although internal refraction within the combustion media was neglected.

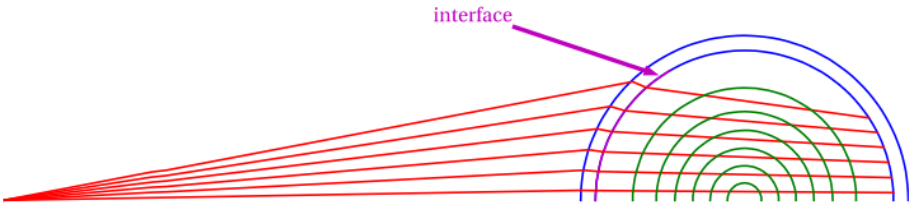

Figure 4.4.: **Schematics of the rays paths used by Fiala. Quartz windows are not shown [3].**

OH* radiation intensity arriving to a pixel was determined by doing the discrete integration of Eqn. (2.14) along the straight path. Emissivity (η_ν) and absorptivity (κ_ν) where determined at each cell center of the CFD domain following three different approaches. These are:

- *Detailed Chemistry Radiation Model (DC)*: the basic assumption is that emission is directly proportional to the concentration of the excited species OH*. For such reasons, OH* must be treated as a separate species and hence the use of the detailed kinetic approach from Eqn. (2.9). The phenomenon of self-absorption is not accounted for in this model ($\kappa_\nu \approx 0$). No information on the emission spectra is used, radiation is only calculated around a center wavelength, $\lambda_c = 308.5\ nm$.

- *Equilibrium Filtered Radiation Model (EFRM)*: assuming thermal equilibrium between the excited and ground state hydroxyl molecules, then concentrations of both are linked by Eqn. 2.11. Emitted radiation is assumed as proportional to OH* concentration. Similarly to the DC model, no spectral information is used, as the free Gibbs energy of the transition ($\Delta_{OH^* \to OH} g^0_m$) is calculated as the energy of a photon of wavelength $\lambda_c = 308.5\ nm$. As OH and OH* concentrations are linked, this model does not require a detailed kinetic scheme. No self-absorption is considered.

- *Spectral Model (SM)*: the emission spectra of the OH molecule is simulated by relying on HITRAN/HITEMP database. It relies on the fundamental assumption of thermal equilibrium. The database provides the list of individual lines at reference conditions as well as their wavenumbers, intensities and expected broadening. A *Python* tool reconstructs the OH spectra following a procedure detailed in Section 4.1.3 of [3]. Emissivity and absorption coefficients at different wavenumbers are determined and provided to the integration of Eqn. (2.14). The resulting spectral intensities are band-pass filtered following Eqn. (3.1) by interpolating from the experimental filter transmittance curve. This model accounts for self-absorption.

As current implementation of SMART accounts for the molecule spectra when generating the pseudo-radiation images, the SM model results from Fiala were deemed to be the fittest for comparison. Also, self-absorption in OH* imaging cannot be neglected as was concluded by Fiala when comparing to experiments, thus both approaches have to account for it to obtain a

reliable benchmarking.

4.1.3. Ray tracing results

The simulations are run over the CFD results from Fiala's work on the pressures (P_c) and mass flow of oxygen ($\dot{m}_O$) listed in Table 4.1. An example of the ray tracing results has been rendered through SMART new implementation in Figure 4.5. In it, the quartz windows and shield are also depicted. Details on the objects definition in the SMART configuration file are given in Appendix A.

Table 4.1.: **Cases over which the algorithm was applied. Denomination refers to the naming convention given in the files of Fiala's work.**

Denomination	P_c $[bar]$	$\dot{m}_O$ $[gr/s]$
LBFSSR03-40-01.00	1.00	40.00
LBFSSR03-40-05.00	5.00	40.00
LBFSSR03-40-10.00	10.00	40.00
LBFSSR03-40-12.00	12.00	40.00
LBFSSR03-40-20.00	20.00	40.00
LBFSSR03-40-30.00	30.00	40.00
LBFSSR03-40-40.00	40.00	40.00

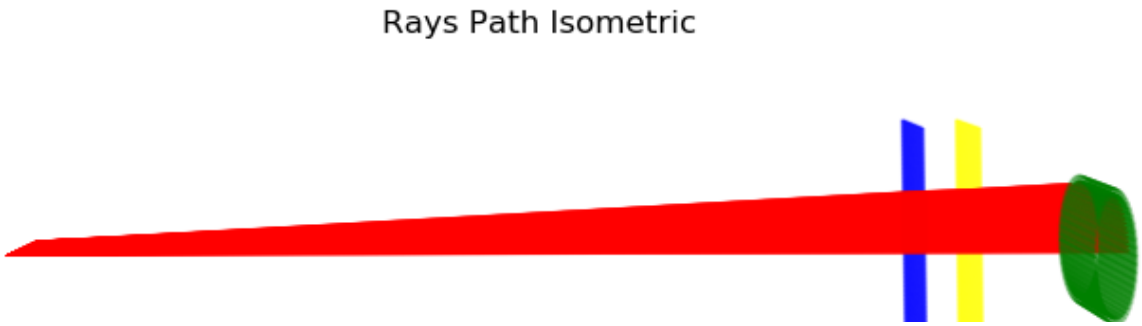

Figure 4.5.: **Geometries and rays instances rendered.**

For case *LBFSSR03-40-01.00* the refraction index field as obtained from Eqn. (2.20) is shown on Figure 4.6a. The side view of the rays trajectory over the combustion domain are shown on Figure 4.7a. In the former it is observed that the refraction index is greater at the vicinity of the oxygen injection plane and decreases downstream. This is possibly due to the density gradients encountered as the combustion products are likely to have lower density due to their higher temperature. Nevertheless, it can be observed that local variations of refraction index occur on the 5th significant figure.

For higher pressures, such as it is in the case of *LBFSSR03-40-40.00* the refraction index field is higher in magnitude, though with changes in the 4th significant figure (see Figure 4.7b).

Rays trajectories for this pressure are shown in Figure 4.7b. Refraction index field is slightly higher due to the higher pressure (p) and consequently higher density encountered. The oxygen core region (blue) is shorter since the mass flow of oxygen remains constant and higher density (ρ_{ox}) implies a smaller injection velocity (v_{inj}), as shown in Eqn. (4.1). In it, A refers to the transversal area of the oxygen lance.

$$v_{inj} = \frac{\dot{m}_{ox}}{\rho_{ox}(p,T)A} \tag{4.1}$$

Figures 4.7a and 4.6b show that rays follow a seemingly straight path within the combustion domain. To explain this observation, an order of magnitudes study is performed.

Starting from the *Eikonal* equation (2.16) and introducing the refraction index field gradient of the form $\vec{\nabla} n(\boldsymbol{r}) \leq \mathcal{O}\left(\frac{10^{-k}}{\Delta x}\right)\hat{n}(\boldsymbol{r})$, where Δx is the mesh characteristic size, $\hat{n}$ the direction unit vector of the gradient at point $\boldsymbol{r}$ and k the magnitude order of change in refraction index. Then:

$$\frac{d\vec{T}}{ds} \leq \mathcal{O}\left(\frac{10^{-k}}{\Delta x}\right)\hat{n}(\boldsymbol{r}) \tag{4.2}$$

with $\vec{T} = n(\boldsymbol{r})\frac{d\boldsymbol{r}}{ds}$. Performing a single point integration around $\boldsymbol{r}$ with an integration step in ray coordinates $0 < \delta s \leq \mathcal{O}(\Delta x)$, consistent with the dimensions of the grid it follows:

$$\vec{T}(s+\delta s) - \vec{T}(s) \leq \delta s\ \mathcal{O}\left(\frac{10^{-k}}{\Delta x}\right)\hat{n}(\boldsymbol{r}) = \mathcal{O}(10^{-k})\hat{n}(\boldsymbol{r}) \tag{4.3}$$

As variations in the refraction index from Figures 4.6a and 4.6b are seen in the 4th and 5th significant figure, then it is valid to assume $n(s+\delta s) \approx n(s) \approx 1$.

$$\begin{gathered} \delta\vec{t} \leq \tfrac{1}{n(s)}\mathcal{O}(10^{-k})\hat{n}(\boldsymbol{r}) \\ |\delta\vec{t}|^2 \leq \mathcal{O}(10^{-k}) \implies |\delta\vec{t}| \leq \mathcal{O}(10^{-k/2}) \end{gathered} \tag{4.4}$$

Where $\vec{t} = \frac{d\boldsymbol{r}}{ds}$ refers to the ray tangent vector and $\delta\vec{t}$ its variation when being integrated between s and $s+\delta s$. Defining the ray coordinate s as the length along the ray curve, it can be proved that $|\vec{t}| = |\frac{d\boldsymbol{r}}{ds}| = \lim_{\Delta s\to 0}|\frac{\Delta\boldsymbol{r}}{\Delta s}| = 1$. Then the maximum angle between $\vec{t}(s)$ and

$\vec{t}(s+\delta s)$ to be expected (θ_c) is bounded by:

$$\tan\theta_c \leq \frac{|\delta\vec{t}|}{|\vec{t}|} \leq \mathcal{O}(10^{-k/2}) \tag{4.5}$$

Eqn. (4.5) leads to the conclusion that the maximum expected change in the ray direction, is of $\mathcal{O}(10^{-k/2})$. For *LBFSSR03-40-01.00* and *LBFSSR03-40-40.00* $k = 4$ and $k = 3$, respectively. Hence, in the former the bound in the deviation is $\mathcal{O}(10^{-2})$ and the latter $\mathcal{O}(10^{-3/2})$, both of which are not detectable to the eye in the scale of Figures 4.7a and 4.7b.

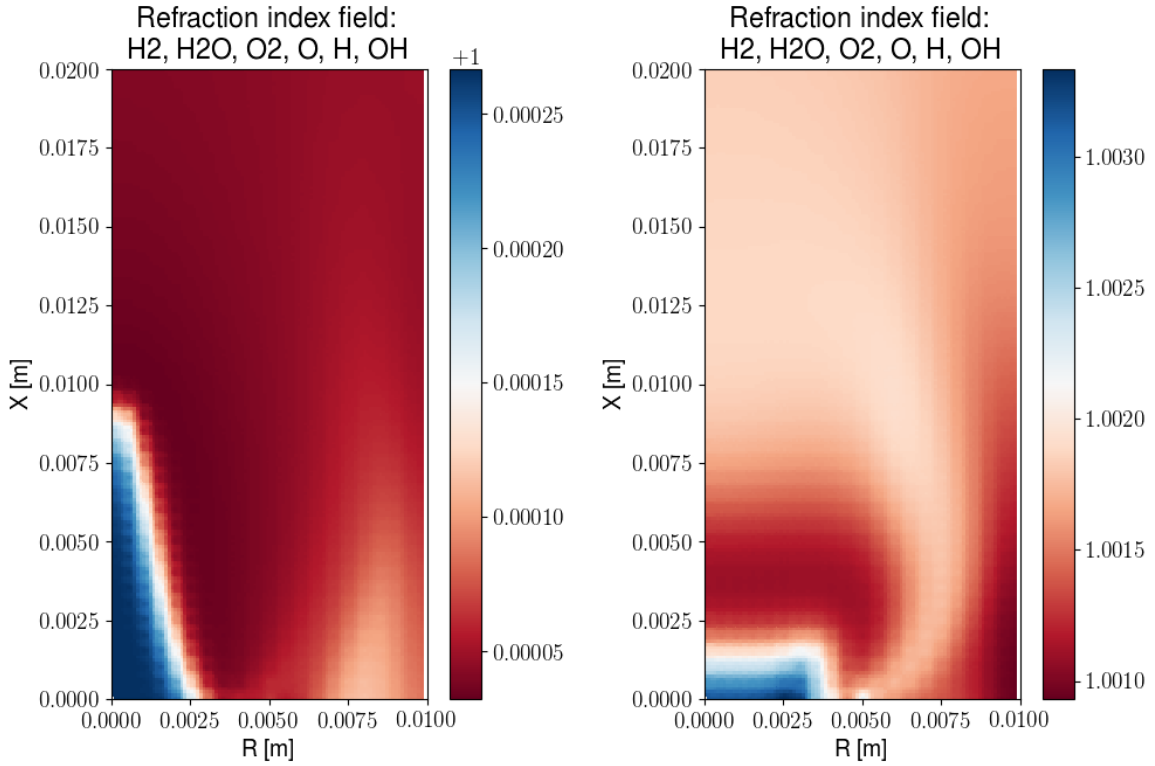

(a) ***LBFSSR03-40-01.00*** (b) ***LBFSSR03-40-40.00***

Figure 4.6.: **Refraction index fields colormaps.**

(a) ***LBFSSR03-40-01.00*** (b) ***LBFSSR03-40-40.00***

Figure 4.7.: **Rays trajectory side-view, x-y plane.**

4.1.4. Radiation modeling comparison

For cases *LBFSSR03-40-01.00* and *LBFSSR03-40-30.00* the direct comparison between the SM model of Fiala and SMART output is shown in Figures 4.8a and 4.9a, respectively. Both methods account for self-absorption and the rays used have been generated in presumably the same conditions. The quantities displayed correspond to the normalized[1] OH^* radiation intensity as collected by the camera. A difference between both fields is shown on the color map of Figures 4.8b and 4.9b. The comparison images and difference plots of other studied pressures have been included in Appendix E.

Figures 4.8a and 4.8a show that the observed flames are similar in shape, however the SM results from Fiala show a flame with slightly greater volume. Potential reasons for the bigger flame volume by the model of Fiala are:

1. Refraction within the combustion domain: as it was shown in Section 4.1.3, for the refraction index field obtained in the combustion domain, the maximum possible local change in direction of the rays is of $\mathcal{O}(10^{-k/2})$, with k being the order of magnitude of change in the refraction index field. In Figure 4.9b for instance, the maximum difference between the two approaches is located at the region of maximum gradients in intensity. This zone is coincidental with a region of high-refraction index gradients. A quantitative analysis should be performed to assess the bending of the rays in the cases presented.

2. SM radiation model: in the present code, the emission and absorption coefficients are obtained from a *Python* wrapped *DLR-TAU* library, inherited from the work of Perovsěk [10]. It is possible that there exist differences in the spectral computations between the *DLR-TAU* library and the tool used by the SM model of Fiala. This question was not resolved within the scope of this work and should be clarified in future work.

3. Rays origin mismatch: in the present work, special care was taken to generate the same rays used by Fiala to perform his simulations. However, differences may occur as it was

[1] Between the maximum and minimum values $\|\phi\| = \frac{\phi - \min\phi}{\max\phi - \min\phi}$.

unclear to the author of this report which method was used by Fiala to estimate the refraction of the rays at the side quartz-windows and quartz shield.

4. The mesh used is too coarse: as for the algorithm, pressure, temperature and mass fraction of species are interpolated from the mesh by means of a **"cKD tree"** with a search depth of 6 (number of points used in the interpolation). If the mesh is too coarse this results in an over-smoothed field. Numerical experiments were done to contrast this hypothesis by resampling the data to a finer mesh. However, no significant difference was detected for the 2x refinement performed.

Figures 4.10a and 4.10b, extracted from [3] show the comparison of the Fiala SM results to the experiments. Even though a direct comparison of SMART to experimental data was not reached, these images are useful to qualitatively assess the performance of SMART with respect to the SM model and experimental data.

In the SM model as noted by Fiala, "radiation peaks a little too far downstream compared to the experiment". Comparatively, in SMART it is seen a smaller flame volume in both cases shown and radiation peaks upstream of SM, thus yielding a closer flame to the experiment. According to Fiala, the downstream peak of SM results are a consequence of the CFD simulations, however results from SMART show, that in spite of using the same underlying data the peak is observed slightly before, thus pointing that the the modeling of radiation may as well contribute to this phenomenon.

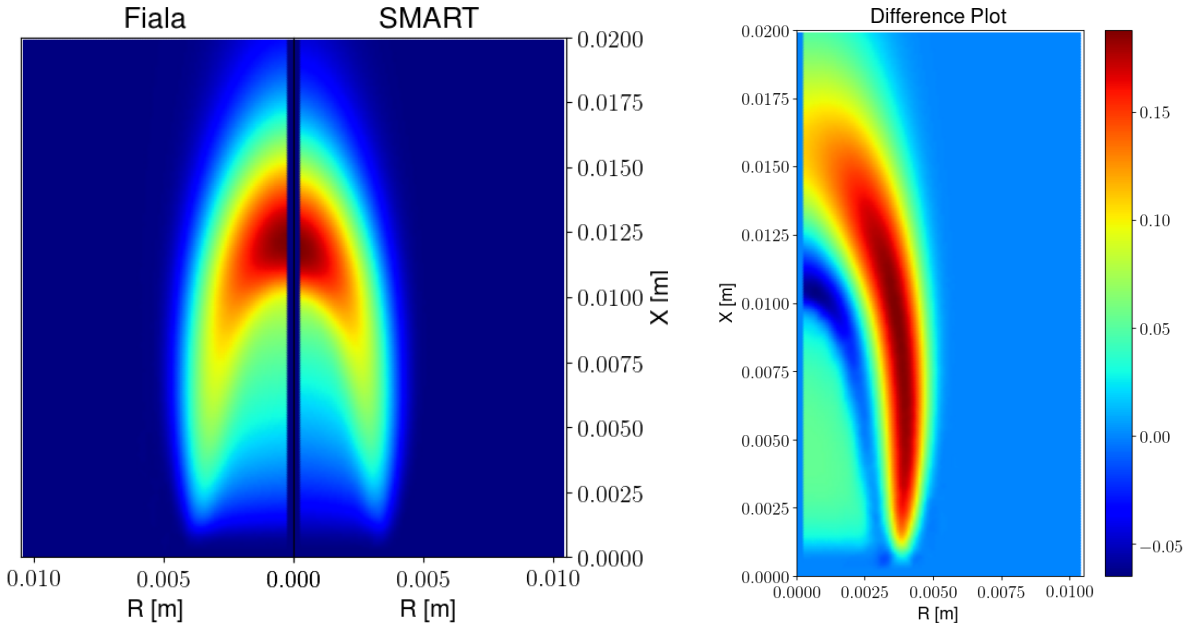

(a) Comparison of normalized OH* radiation intensity, Fiala SM-SMART tool.

(b) Difference, normalized OH* radiation intensity.

Figure 4.8.: Results *LBSSR03-40-01.00* case.

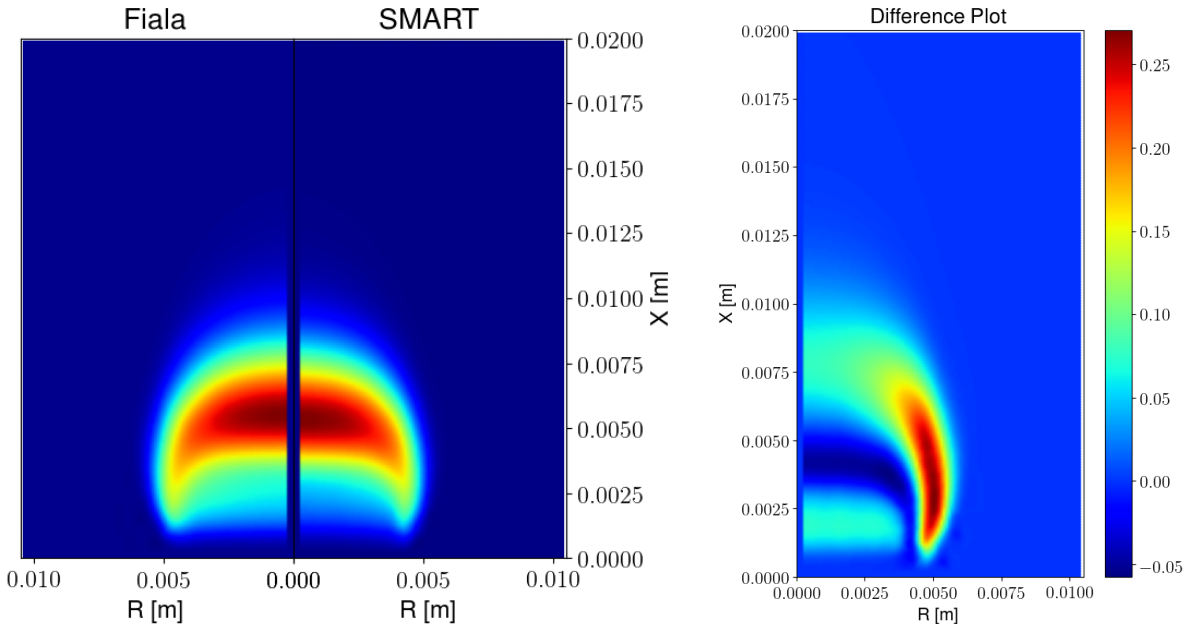

(a) Comparison of normalized OH* radiation intensity, Fiala SM-SMART tool.

(b) Difference, normalized OH* radiation intensity.

Figure 4.9.: Results *LBSSR03-40-30.00* case.

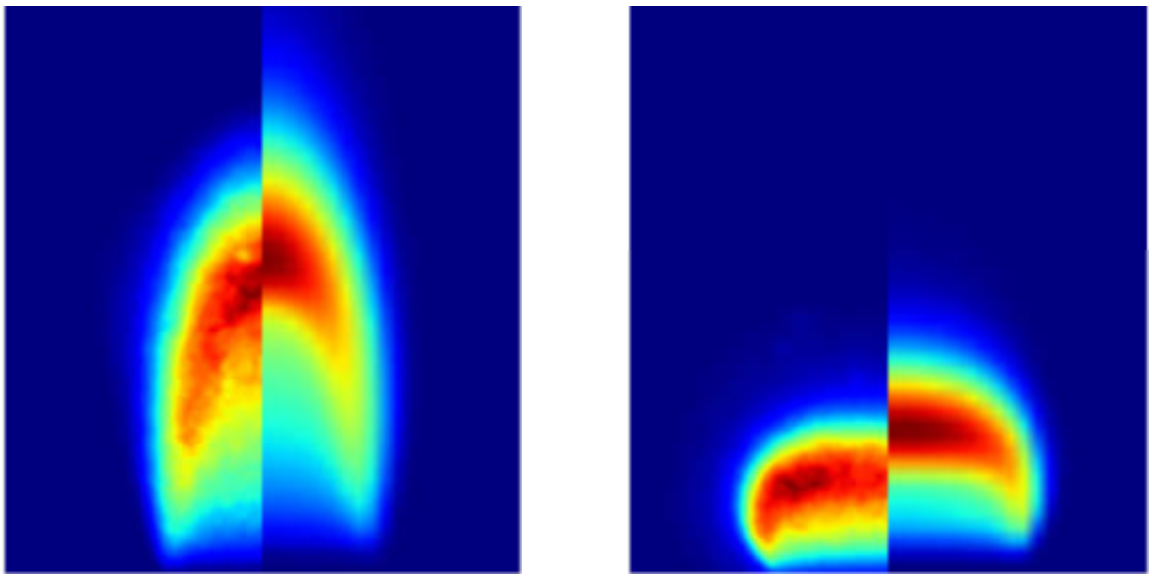

(a) ***LBFSSR03-40-01.00*** **case.** (b) ***LBFSSR03-40-30.00*** **case.**

Figure 4.10.: **Fiala results, experiment (left) and SM model (right) [3].**

4.2. Test case B: REST HF-9 unsteady flame response

Another application case of the SMART tool which has been studied in detail is the unsteady simulation of the OH* radiation flux collected by an optical probe in DLR's *BKD* combustor. The latter is placed at the European Research and Technology Test Facility P8 for cryogenic combustion. It consists of a multi-element injector head, a measurement ring, a 200-mm-long cylindrical chamber segment and a convergent-divergent nozzle. The inner diameter of the chamber is 80 mm and the nozzle throat diameter is 50 mm [1]. A sketch of the thrust chamber is shown on Figure 4.11a.

Propellants are injected through 42 shear coaxial injection elements distributed in three rings of 62, 41 and 21 mm in diameter, as shown on Figure 4.11b. BKD is a relevant test case for the study of combustion instabilities as it presents self-excited instabilities [1] and its operating conditions and multi-element injection make it resemble the closest to a full-scale combustion chamber.

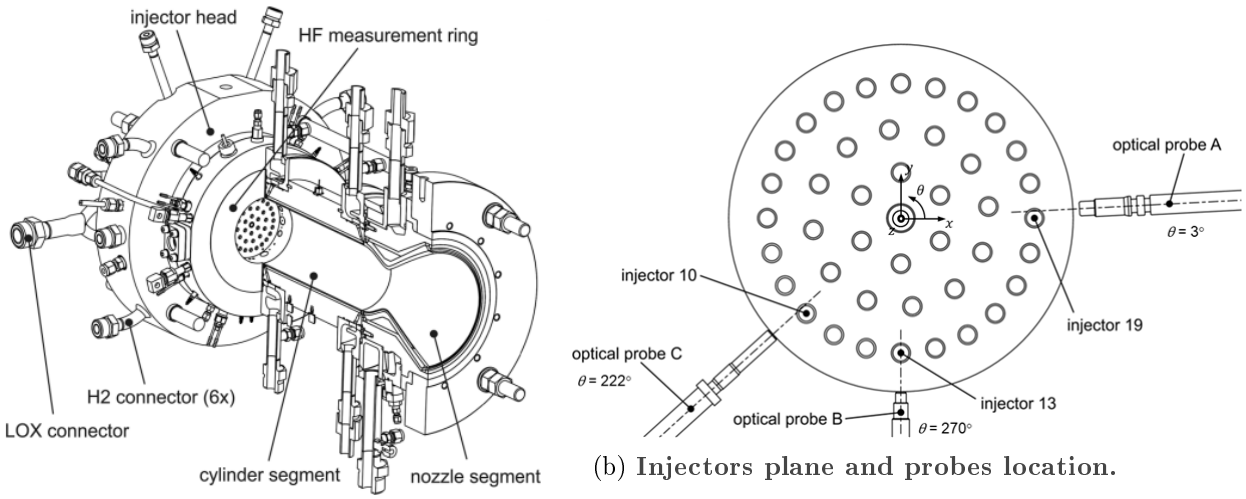

(a) **Thrust chamber BKD [1].**

(b) **Injectors plane and probes location.**

Figure 4.11.: **BKD experimental combustor.**

LOX-H2 CFD URANS simulations carried out by Tonti have been the source of the CFD solution fields for the present application. These were performed over a 6.2 mm radius axisymmetric mesh centered in BKD's injector 10 axis. A fluctuating pressure field disturbance ($p^{'}$) was imposed on the domain boundary following the eigenfrequencies calcualted from an acoustic analysis of a steady-state solution. The pressure field is centered around a mean value of pressure of the chamber ($\overline{p}$). The first transverse mode (1T) is located at 11700 Hz. The amplitude (A) of the disturbances is given by the experimental data. The OH mass fraction steady-state solution is shown in Figure 4.12.

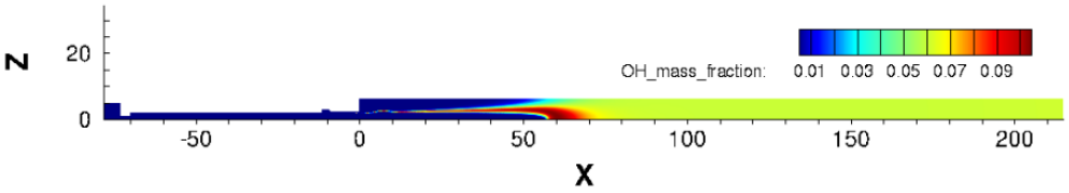

Figure 4.12.: **Steady-state OH mass fraction solution. Provided by Tonti.**

The axial distribution of the disturbance (x direction with L being the chamber length) is given in Eqn. (4.6).

$$\begin{cases} p = \overline{p} + p^{'} \\ p^{'} = A\cos(2\pi f t)\cos\left(\dfrac{\pi x}{2L}\right) \end{cases} \tag{4.6}$$

Hosted in the measurement ring, the optical probe C (see Figure 4.11b) is conveniently oriented

and located at 5.5 mm from the injection plane. Its objective is to capture the radiation being emitted from the shear-layer of injector 10. For such reason, it was decided to attempt the estimation of the OH* radiation by means of the SMART tool.

4.2.1. Probe modeling

Prior to running the algorithm over the CFD solution from Tonti, it is necessary to derive a model of the probe which overlooks to injector 10 (Probe C) that is compatible with SMART's hypotheses' (ray-tracing based). An optical probe is a sensor which collects the incoming radiation within its view angle and later the electromagnetic energy flux is transferred through an optical fiber to a filter and a photomultiplier.

Thus, it is necessary to determine first the view angle of the probe. Three sections are identified based on the internal diameter of the probe: the top corresponds to a sapphire rod[2] which allows the radiation to pass while keeping air tightness; the center corresponds to a contraction in diameter which is empty and the bottom is an expansion which ultimately leads to the fiber-optics face. The walls are considered opaque and so any internal reflection is neglected.

The view angle of the probe is determined by the limit rays that reach the circular boundary of the fiber-optics face. A schematics of the simple computational model built is shown in Figure 4.13. Red dashed lines correspond to the limit rays which reach the fiber face whereas green dashed denote the apparent observation cone of the probe[3]. The cone angle was determined to be 2.39°.

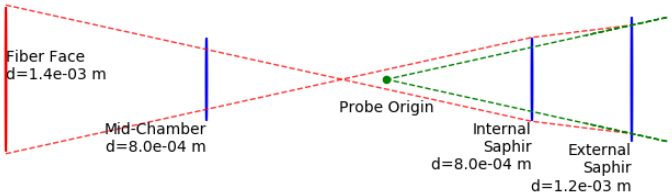

Figure 4.13.: **Probe C simplified schematics with extreme rays. Figure not in scale.**

With this in mind, the probe is approximated to an observation cone with a vertex B ("Probe Origin" in Figure 4.13) which serves as a sink for radiation. Radiation absorption along the sapphire rod is not considered. With this approximation, the total radiation flux $[W/m^2]$ which reaches the sink B is given by Eqn. (4.7). The probe surface is assumed to be non-reflective.

$$\phi(B) = \int_0^\infty \int_\Omega \tau_{\nu,OH} I_\nu(B, \vec{u}) |\vec{u} \cdot \vec{n}_B| d\Omega d\nu \tag{4.7}$$

[2]The refraction index of Sapphire considered is $n_{sapphire} \approx 1.8$ for a reference wavelength $\lambda_{ref} \approx 300\ nm$. Generated from [11].

[3]In reality, the sapphire rod has a small chamfer at one end which has been ignored for the present calculation.

where τ_ν, $\vec{u}$, $\vec{n}_B$, Ω are the probe's transmissivity function of the wavenumber ν, the radiation direction vector, the normal unit vector of the surface at point B (considered as the probe's pointing vector) and the solid angle given by the observation cone, respectively. The spectrum of interest is the one associated to OH* radiation, therefore τ_ν is taken as a band-pass filter for the wavelengths of interest (τ_{ν,OH^*})[4].

Introducing a proper partition for the solid angle such that $\Omega = \bigcup_i \Omega_i : \Omega_j \cap \Omega_k = \phi$; replacing by the definition of solid angle (see Figure 4.14) through elevation complement angle (θ) and azimuth (φ) and conveniently defining a normal vector $\vec{n}_B$ as the zenith direction ($|\vec{u} \cdot \vec{n}_B| = \cos\theta$) then,

$$\begin{aligned} &\phi_{OH^*}(B) = \textstyle\sum_i \int_{\Omega_i} \left(\int_0^\infty \tau_{\nu,OH^*} I_\nu(B,\vec{u}) d\nu \right) |\vec{u} \cdot \vec{n}_B| d\Omega \\ &\implies \phi_{OH^*} = \textstyle\sum_i \int_{\Omega_i} I(B,\vec{u}) |\vec{u} \cdot \vec{n}_B| d\Omega \\ &\implies \phi_{OH^*}(B) = \textstyle\sum_{i,j} \int_{\varphi_j}^{\varphi_{j+1}} \int_{\theta_i}^{\theta_{i+1}} I(B,\vec{u}) \sin\theta \cos\theta d\theta d\varphi \end{aligned} \tag{4.8}$$

Defining $\Delta\varphi_{j+1,j} = \varphi_{j+1} - \varphi_j$, $\Delta\theta_{i+1,i} = \theta_{i+1} - \theta_i$ and performing a single Gauss Point integration,

$$\phi_{OH^*}(B) \approx \sum_{i,j} I(B,\vec{u}_{i,j}) \Delta\varphi_{j+1,j} \sin\left(\Delta\theta_{i+1,i}\right) \sin\left(2\theta_{i+\frac{1}{2}}\right) \tag{4.9}$$

The term $I(B,\vec{u}_{i,j})$ can be replaced by the associated OH^* radiation of a single ray whose incidence direction is given by the pair $\theta_{i+\frac{1}{2}}$, $\varphi_{j+\frac{1}{2}}$. Additionally, if $\Delta\theta_{i+1,i} << 1 \implies \cos\Delta\theta_{i+1,i} \approx 1$, assumption valid for this analysis. Replacing with the solid angle definition and mapping the pair $i,j \to k$ where k represents a single ray, then,

$$\phi_{OH^*}(B) \approx 2 \sum_k I(B,\vec{u}_k) \Delta\Omega_k cos(\theta_k) \tag{4.10}$$

In Eqn. (4.10), $I(B,\vec{u}_k)$, $\Delta\Omega_k$ and θ_k represent then the OH* incoming radiation, solid angle portion and elevation complement angle associated to ray k, respectively. Each ray is determined by its azimuth and elevation complement angle which describe the corresponding solid angle. The discretization proposed considered a total of 100 rays, with even angular spacing in the azimuth discretization ($\varphi \in [0, 360°]$) and the elevation complement ($\theta \in [-2.39°, 2.39°]/2$). Such a small number of rays is used due to the large computing time (≈ 4 *days*) required to process the ≈ 2000 time-steps from the transient simulation described above and performed by Tonti. A code profiling study on the tool is presented in Section 4.3 to explain the origin of the large computing times involved.

[4] For the results obtained in effect the filter function used by Perovsëk in his analysis of *BKH* was used. However, a squared band-pass filter can be easily implemented in the program.

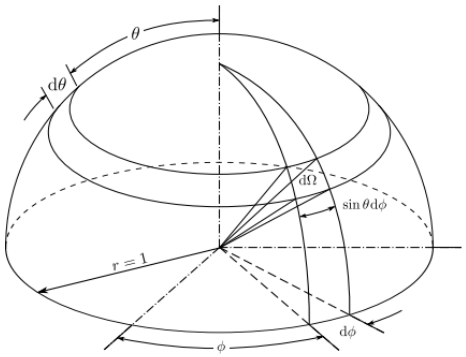

Figure 4.14.: **Infinitesimal solid angle on a unit radius hemisphere [10].**

Having provided a model for the probe, the configuration file of the SMART tool was assembled. Appendix B provides more details on the case definition. The algorithm was run on the ≈ 2000 time-steps and later results were processed to compute the OH* radiation flux.

Figures 4.15a and 4.15b show the rendered side view of the trajectory of the rays and the relative location of the *BKD* chamber and CFD domain boundary. In the latter, the probe's cone of observation vertex is identified by a green dot labeled "Probe Origin". It is important to mention that radiation coming from other injector flames is not accounted for in the calculation as it is assumed that the larger part of it will only originate at injector's 10 flame.

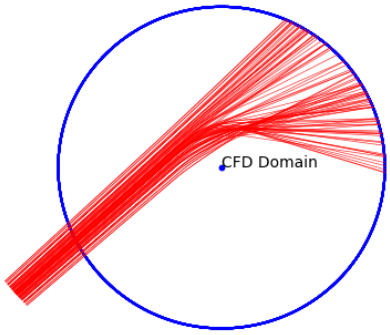

(a) **Rays trajectory within the CFD domain (blue), side view.**

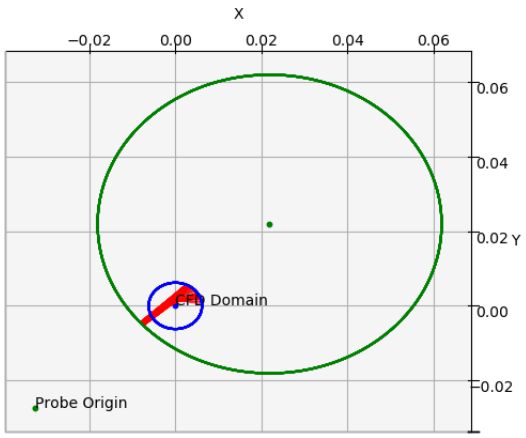

(b) **Geometries relative position, BKD chamber (green), CFD domain (blue).**

Figure 4.15.: **Geometries rendering, HF9 REST case.**

4.2.2. OH* radiation analysis

The OH* radiation flux signal estimated by SMART (ϕ_{OH^*} SMART) to be collected by the probe is shown in Figure 4.16 alongside the pressure disturbance signal[5] ($p^{'}$). For convenience, the OH* radiation flux signal has been normalized by its respective mean value ($\overline{\phi}_{OH^*}$).

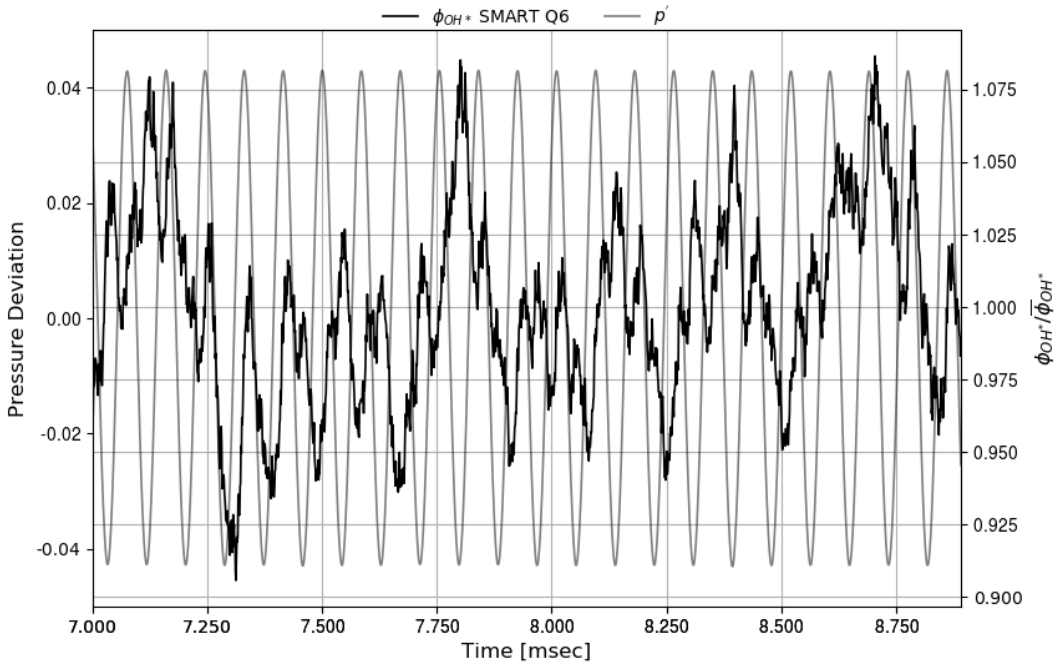

Figure 4.16.: **OH* radiation flux signal and average pressure disturbance.**

Figure 4.16 shows that radiation has a major frequency component of the same value as the pressure with a phase difference smaller than $\frac{\pi}{2}$. Slower and higher frequency components are also visible. A priori, the source of these is unknown. A simple PSD analysis of the signal is superposed with those of the normalized average pressure field ($\overline{p}$) and normalized average density field ($\overline{\rho}$). The frequency $f_0 \approx 11.8$ kHz, close to the excitation frequency (1T), is present in all the signals. In all of the signals plotted, additional peaks corresponding to overtones of f_0 are observed.

The normalized average pressure signal ($\overline{p}$) between the first peak at f_0 and the first overtone $f_1 \approx 2f_0$ has a power ratio of $\frac{P_{xx}(f_0)}{P_{xx}(f_1)} \approx 10^5$. Knowing that the power of the signal is proportional to the square of the amplitude (A) then $A_{\overline{p}}(f_1) \approx 10^{-5/2} A_{\overline{p}}(f_0) = 0.0032 A_{\overline{p}}(f_0)$. The definition given for $p^{'}$ and $\overline{p}$ implies that $p^{'} \propto \overline{p}$, then it yields $A_{p'}(f_1) \approx 0.0032 A_{p'}(f_0)$. From Figure 4.16, $A_{p'} \approx 0.04 \implies A_{p'}(f_1) = 1.2 \times 10^{-4}$. In the scale of the graph of Figure 4.2.2, this order of magnitude is not observable, thus explaining why the overtones of $p^{'}$ are not detectable in

[5] The pressure disturbance is determined as the deviation from the mean pressure of the field average pressure divided by the average pressure, at a given instant.

the plot. On the contrary, for the OH* radiation flux signal, the peaks shown in the PSD are not significantly distant in power, which explains why a more complex shape is observed in Figure 4.16.

Laying the focus in the $[0-10]$ kHz interval, the OH* radiation flux signal shows an additional peak at ≈ 5.4 kHz. Even though of unknown origin, it is suspected that this peak corresponds to the first longitudinal mode (1L) of the LOX post, as a peak in a similar frequency was detected in the experiments carried by Armbruster et al. [1] in the BKD combustor. Gröning et al. [4] determined from experiments the wavenumbers (k) of the different modes of the oxygen injectors. For the 1L mode, $k_{1L} = 42.7$ 1/m. From the simulations of Tonti, the mean value LOX speed of sound at the injector is $c_{LOX,inj} \approx 788$m/s. Therefore the predicted 1L mode frequency is given by Eqn. (4.11) resulting very close to the frequency found in Figure 4.17.

$$f_{1L} = \frac{k_{1L} c_{LOX,inj}}{2\pi} \approx 5.4 \text{ kHz} \tag{4.11}$$

This mode of the LOX post is present as the second overtone frequency of it is very close to the excitation frequency used f_0. As a consequence, the LOX hydrodynamics is excited causing the 1L mode to appear in the frequency collected by the radiation. This peak explains the oscillations in the OH* radiation flux signal seen on Figure 4.16 which are slower with respect to pressure disturbance signal.

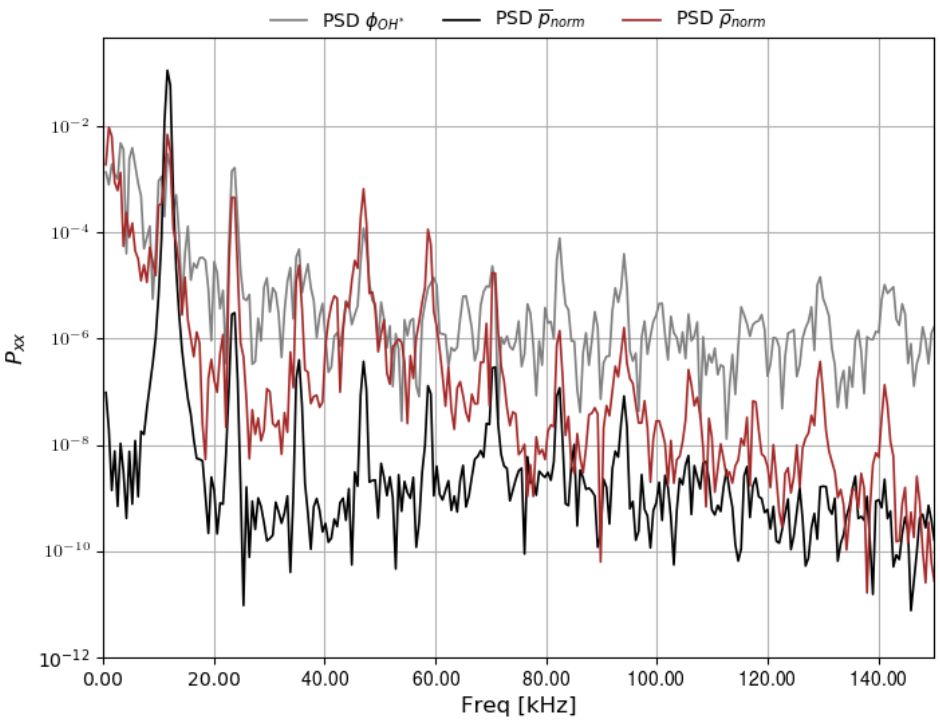

Figure 4.17.: **PSD of OH* radiation signal, average pressure field and average density field.**

4.2.3. SMART - Line-of-Sight Comparison

Line-of-sight () integration refers to the case where the refraction of the rays within the combustion media is not considered. Thus, rays are taken as straight lines which cross the combustion media and consequently the radiative transfer equation (2.14) is integrated over a straight path. A plot of the line-of-sight integrated (ϕ_{OH^*} LOS) and SMART (ϕ_{OH^*} SMART) OH* estimated radiation flux signals is shown in Figure 4.18. For convenience, both signals have been scaled by their respective average values ($\hat{\phi}_{OH^*}$).

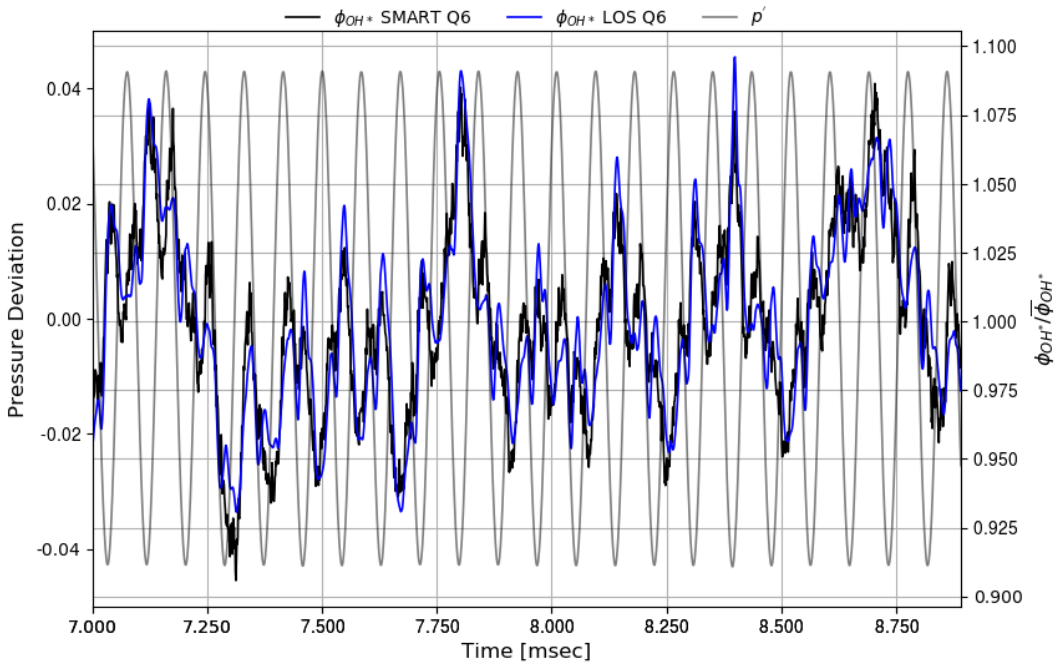

Figure 4.18.: **OH* radiation flux signal comparison, SMART and LOS.**

Overall, the LOS signal follows the trend of the SMART prediction, however, the latter appears as noisier with a more complex frequency composition. A difference between both signals adjusted by the ϕ_{OH*}SMART average is shown in Figure 4.19. The right axis scale is given as a percentage of the average OH* radiation flux predicted by SMART. A PSD of both signals alongside their difference adjusted by the SMART mean value is given in Figure 4.20.

From Figure 4.19 it is observed that the maximum difference attained between the SMART and LOS approaches spans between -4% and 3% of the average radiation flux value. The difference between both has a major frequency component coincidental with the excitation frequency f_0. This is observed in the PSD of the difference signal, which peaks at 11.8 kHz. The PSDs of both the SMART and LOS results are similar until ≈ 90 kHz, point in which the PSDs start to differ, with the LOS decreasing in power. Even though the PSD results are similar, it is seen that the frequency composition of their difference peaks at the different overtones of f_0.

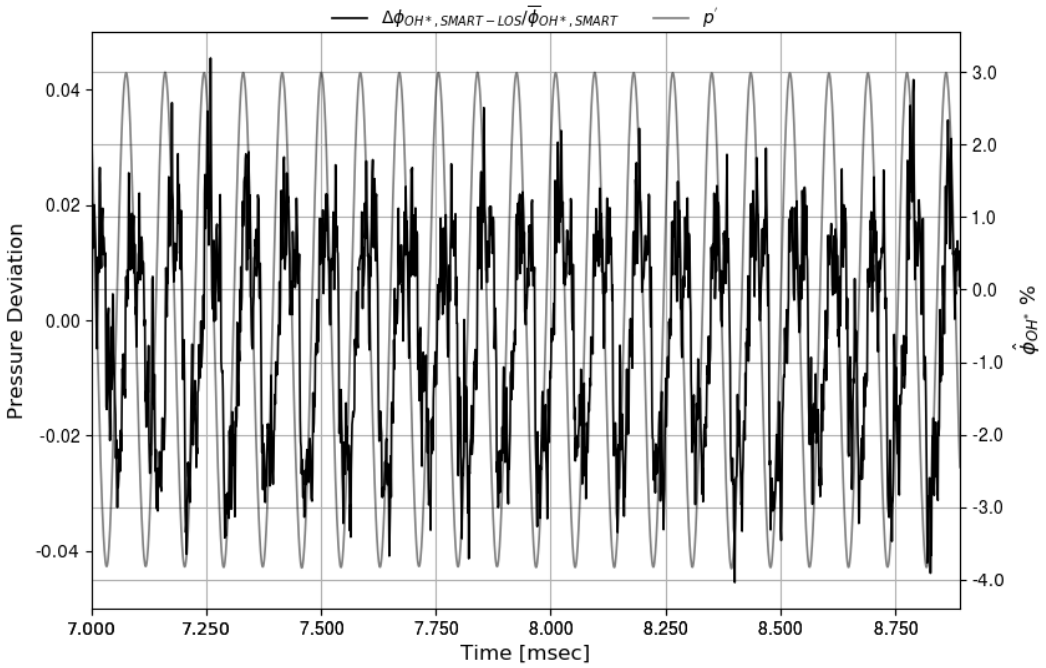

Figure 4.19.: **OH* radiation flux signal difference SMART-LOS.**

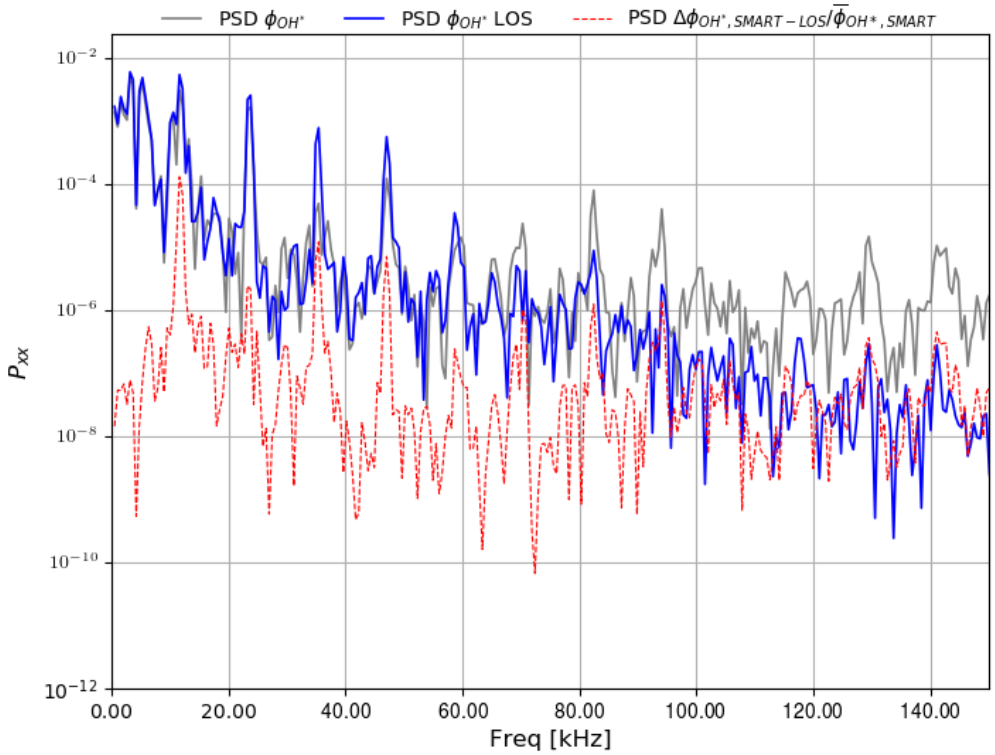

Figure 4.20.: **PSD of OH* radiation signals SMART-LOS and difference.**

When superposing animations of the rays and the density field it was found that part the radiation flux oscillations might originate in the interaction of rays with the wakes that develop in the boundary of the LOX jet. Figures 4.21 show snapshots of the density field in the vicinity of the probe. The plot axes correspond to cylindrical coordinates. Rays paths have been projected into these coordinates. Additionally, radiation intensity derivative with respect to the ray coordinate is shown in *jet* color-coding along its trajectory. Snapshots were taken a time-steps equivalent to 0, $\pi/2$, π and $3\pi/2$ of phase argument of the pressure deviation signal ($\alpha_{p'}$) from Figure 4.16. Similarly, Figures 4.22 show the snapshots of the OH mass fraction field.

Since the probe directly points to the shear layer of the LOX core of injector 10, most of the rays pass through this region. As shown in Figures 4.21, a portion of the rays bundle crosses the LOX jet wake. The shear-layer is a complex turbulent structure with intense density gradients both in the radial direction as well as in the axial direction. These structures have a frequential composition that count with both low and high frequencies. High density gradients result in large refraction index gradients causing strong bending of the rays. When interacting with the wake the rays bend not only radially but axially, as observed in the snapshots of the density field. Consequently, their intersection with the OH rich layer, where emitting radicals are present, changes, as shown in the snapshots from Figure 4.22.

Animations show that there is a high frequency component in the rays movement as well as a strong "slow" frequency coincidental to the traslation movement of the wake and with f_0. This would explain why the SMART-LOS results difference peaks at this frequency.

Variations in time of the thickness or location of the OH rich layer where not found visually significant from the snapshots in Figure 4.22. Nonetheless, to complement this qualitative analysis, a Dynamic Mode Decomposition (DMD) [12] is recommended. In order to investigate the spatial distribution of the dominant frequencies and study in particular the shear-layer composition as well as the OH rich layer. Due to time constraints this study was not performed.

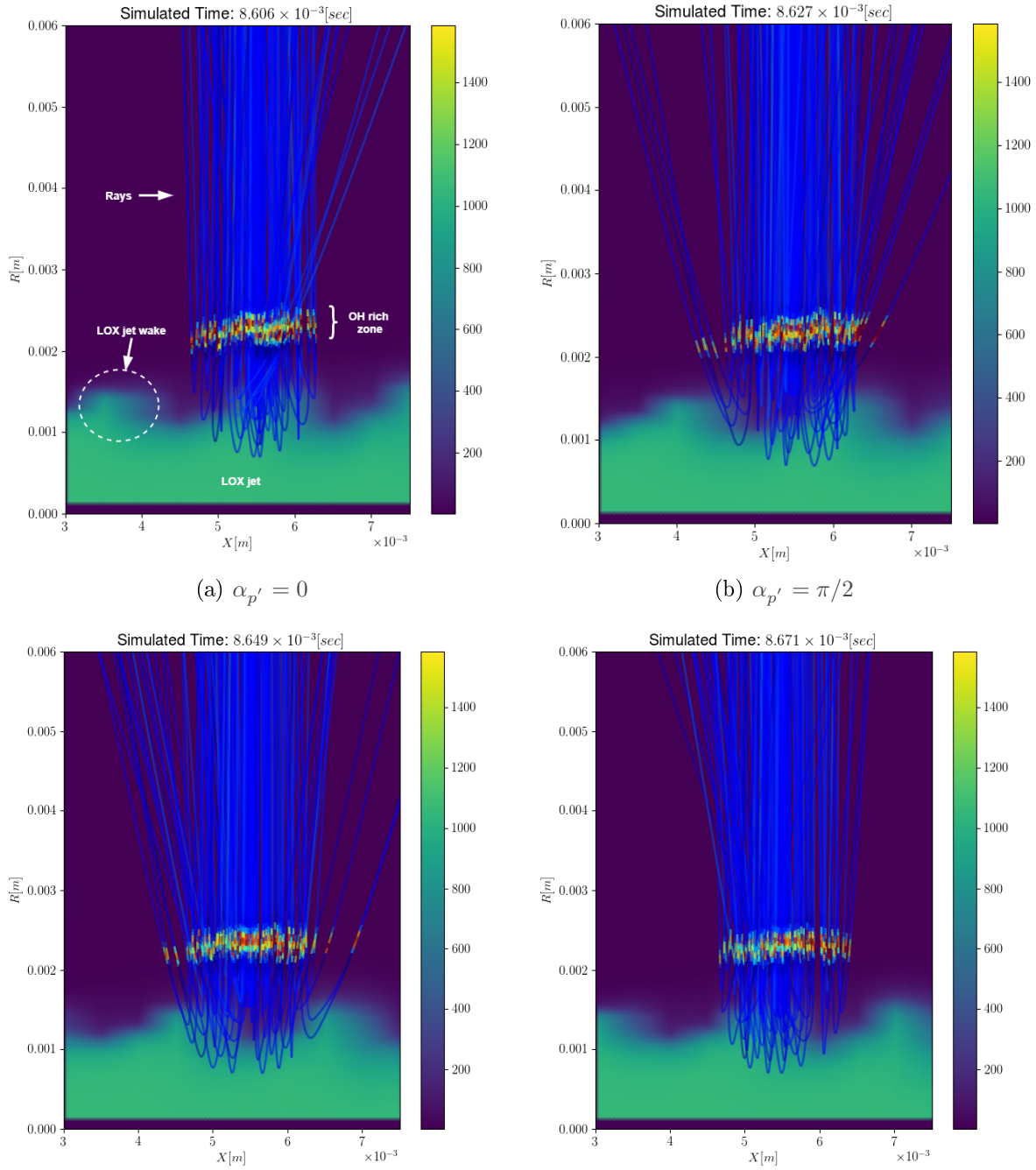

(a) $\alpha_{p'} = 0$ (b) $\alpha_{p'} = \pi/2$

(c) $\alpha_{p'} = \pi$ (d) $\alpha_{p'} = 3\pi/2$

Figure 4.21.: **Density field $[kg/m^3]$ snapshots in cylindrical coordinates with projected rays path.**

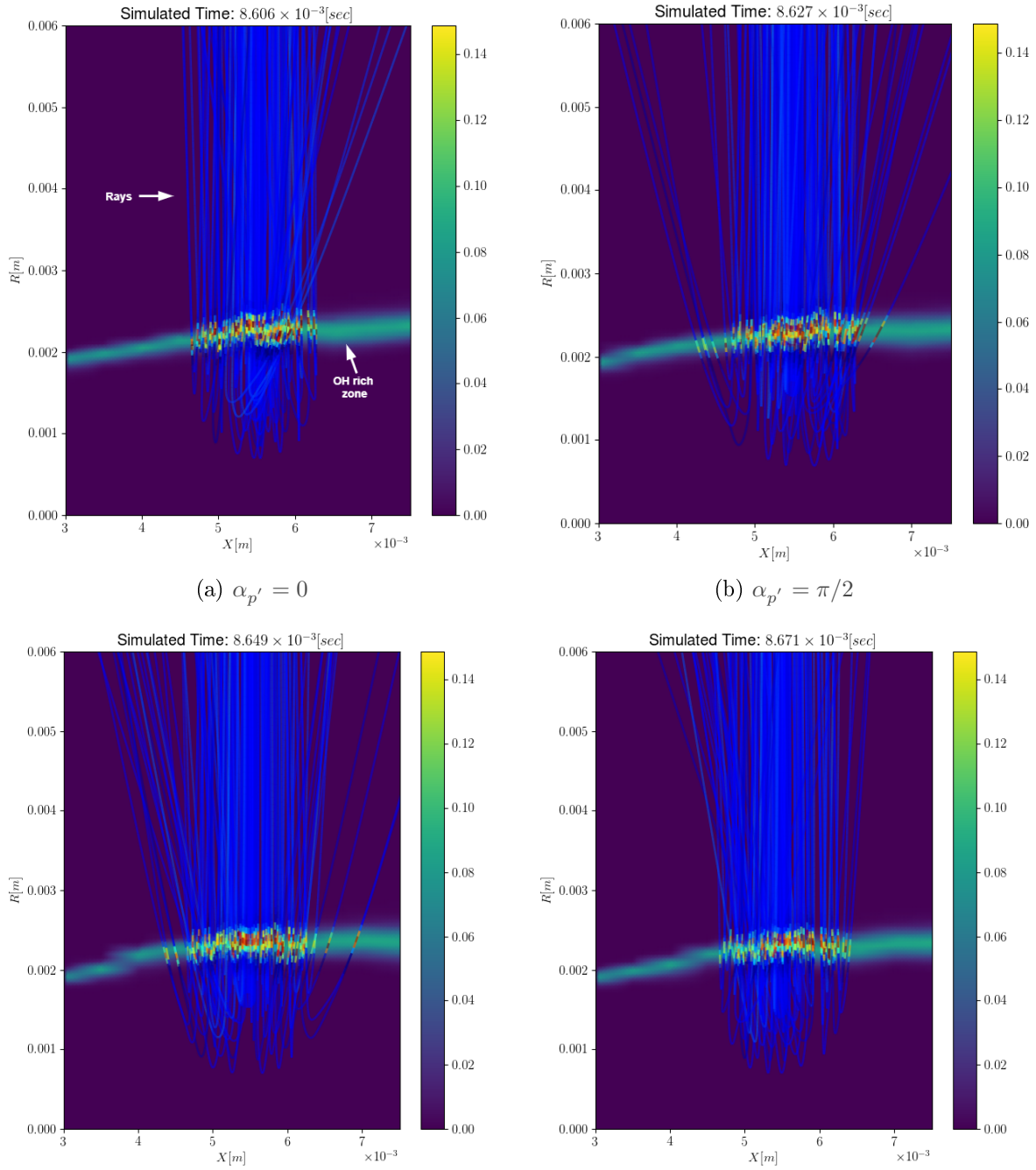

(a) $\alpha_{p'} = 0$

(b) $\alpha_{p'} = \pi/2$

(c) $\alpha_{p'} = \pi$

(d) $\alpha_{p'} = 3\pi/2$

Figure 4.22.: **OH mass fraction field snapshots in cylindrical coordinates with projected rays path.**

4.2.3.1. Numerical studies

The SMART tool [10] requires the spatial interpolation of different scalar quantities (pressure, temperature, mass fractions, refraction index, etc.) from a cloud of data-points[6]. The tool that is used is a **"cKD tree"** which retrieves the nearest points in a cloud to a given point of interest. The data associated to these points are interpolated by inverse distance pondering as shown in Eqn. (4.12) where d is the point-to-point distance and p is a penalization exponent. For the present project $p = 2$ to better deal with high gradient regions. In the work of Perovsěk [10] it was taken $p = 1$.

$$\varphi(\boldsymbol{r}) = \frac{\sum_i^k \frac{\varphi_i}{d_i^p}}{\sum_i^k \frac{1}{d_i^p}} \tag{4.12}$$

The number of points considered in the interpolation k is the search depth or query depth. A study of the impact of this parameter was performed. Figure 4.23 shows that normalized OH* radiation flux signal for search depths of 6 ($Q6$) and 12 ($Q12$) are distinctively different in phase. This phenomenon is purely numerical and requires clarification in future work before the tool can be routinely applied to study flame dynamics. One hypothesis is that the more points are taken within the same grid, the farther away points and information are considered to perform the interpolation. In a steady-state problem this would result in an smoothing of the field. However, in spatio-temporal data this could imply that frequencial information from nearby zones is taken into consideration. If such is the case, the solution could improve by increasing the penalization factor, though at the expense of computing times.

[6] This is how the data is treated at an algorithm level, although in reality each data-point in the cloud is data from a mesh, either structured or unstructured.

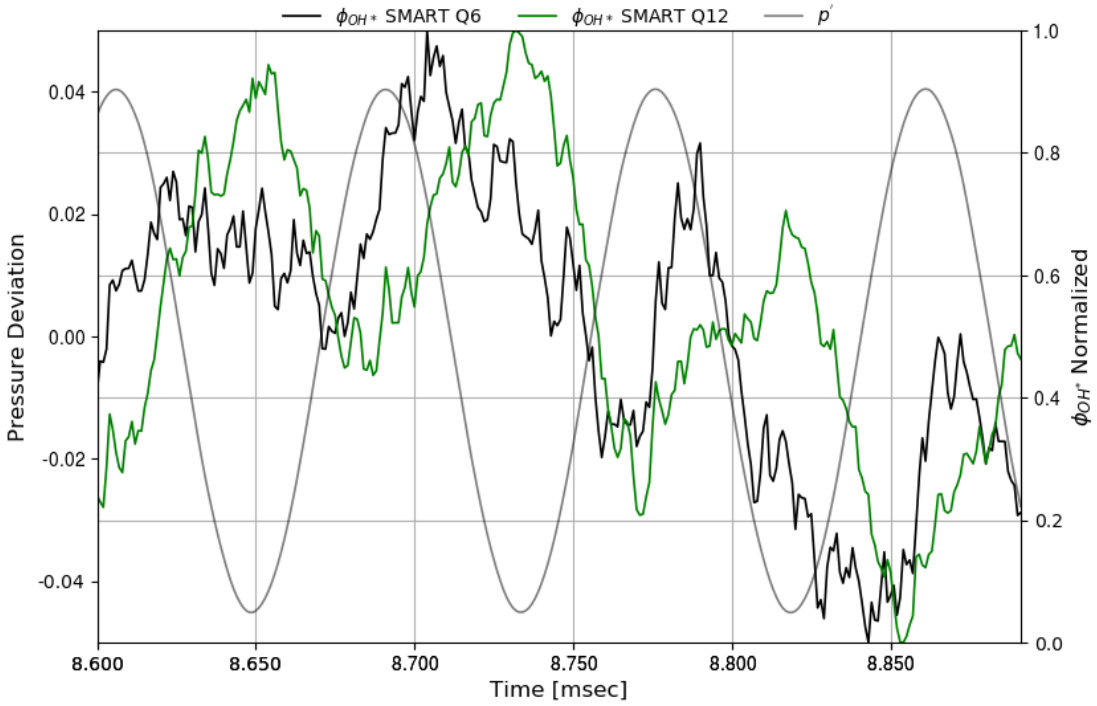

Figure 4.23.: **OH* radiation flux comparison for different "ckD tree" search depths.**

4.3. Code profiling study

A profiling analysis was performed on a non-parallel version of the code to understand better the time consumption of the different sections as it was detected at an early stage the time-consuming nature of the SMART tool (as Perovsĕk already mentioned in [10]). Taking the Fiala configuration with a reduced number of rays (20) as test specimen, the most relevant results are presented in Table 4.2.

Table 4.2.: **Code profiling most relevant statistics.**

# calls	Total Own Time [sec]	Total Own Time [% of Total Time]	Cummulative Own Time [% of Total Time]	Function Name
3720	44.325	38.954	38.954	*radiative_spectra_for_gas_state*
3720	22.464	19.742	58.696	*evaluate_spectra*
111622320	17.045	14.98	73.676	*PySwigIterator_next*
111622320	16.205	14.241	87.917	*next*

From the table, own time is interpreted as the time spent in the function without considering

time spent in other nested functions. From this, it can be observed that ≈ 87.917 % of the simulation time is spent in the four listed functions. All of these are linked to the *Python* wrapped *TAU* libraries which provide the emissivity and absorption coefficients as a function of wavenumber for the OH^* radiation intensity calculations.

The most consuming and is the calculation of the coefficients η_ν and κ_ν, corresponding to the function *radiative_spectra_for_gas_state*. The function *evaluated_spectra* is linked to data preparation for the calculation and *PySwigIterator_next* and *next* refer to numerous calls to an iterator for data exchange between the dependency objects and the *Python* objects requiring that data in memory.

An important conclusion from this analysis is that performance enhancement of the code requires thus a more comprehensive approach of the spectral modeling, now limited to the software dependencies mentioned. First, by improving the data-exchange mechanism between the dependencies and the software, possibly by passing python readable arrays as whole objects rather than looping value by value. Second, by recoding the library to be developed in *Cython*, as other known-for-performance libraries like *numpy* or *scipy*.

The performance conundrum is, the main obstacle in the applicability of the algorithm for future combustion instabilities studies involving transient CFD simulations.

5. Conclusions

Over the scope of this project, the focus has been laid on the expansion and application of an algorithm to model OH* radiation (SMART) from the CFD of hydrogen-oxygen combustion. The importance of the availability of such tool lies on its relevance to validate CFD codes. Additionally, comparison of simulation with experiments, provides further insights on the underlying mechanisms and outcomes of physical phenomena. It is of particular interest, the study of combustion instabilities that occur inside LREs.

The core of the work done has been the generalization of the SMART tool, originally developed by Perovsěk [10] for the estimation of the OH* radiation intensity over a rectangular cross-section domain with rectangular windows. The approach taken was the complete redesign of the software by switching to an object oriented paradigm with a design of an architecture that bears in mind the requirements of this project.

The architecture presented proved satisfactory in terms of fulfillment of requirements. Segregation and single-responsibility design principles were respected at all times. As a consequence, the architecture is flexible to be easily expanded to other combustor geometries, optical devices, mixtures, and interpolation schemes. Future development times are expected to be reduced significantly due to this decision.

The platform chosen was *Python 2* as some of the external dependencies were not compatible with *Python 3*. Nonetheless, special care was taken to have a cross-compatible deliverable with exception of the dependencies. A migration to *Python 3* should be considered in future work. Additionally, all of the code's sections have been successfully parallelized although it remains necessary to conduct performance studies to assess the speed increase of it and scalability to larger CPU clusters than the one used in this project (8 physical cores desktop computer).

As for the application of the tool, whose results were explained in Section 4, the following remarks can be listed.

1. Radiation profiles obtained by the tool on Fiala's cases match the flame shape. However, flame volume is underestimated with respect to the latter's "Spectral Model" (SM). Potential reasons for such phenomenon may lie in differences in the modeled emission spectra of the hydroxyl molecule, rays refraction within the combustion chamber and quartz windows or used interpolation schemes. Future work should address the source with a more detailed comparison to experimental results.

2. For test case B, a simple model for an optical probe which accounts for the internal refraction that occurs in the sapphire rod was developed. The observation cone angle obtained is 2.39°. A method for estimating the OH* radiation flux is proposed by linking it to the ray concept.

3. Estimated OH* radiation flux frequency composition of the probe is studied. The signal has a major component at the excitation frequency of the pressure field. Additionally, a lower frequency peak is observed at ≈ 5.4 kHz which is suspected to correspond to the 1L mode of the LOX post, as this has been modeled in the URANS simulations performed by Tonti. Predominant higher frequencies observed were seen to be overtones of the excitation.

4. Comparison between the SMART and line-of-sight (LOS) results show that both follow a similar trend. The former however presents higher frequency components. A difference between the two shows that the maximum deviation is $\approx 4\%$ of the mean radiation flux. The difference has a major component in the excitation frequency and higher components of smaller power. A PSD analysis determined that the inclusion of refraction in the calculation impacts the spectral power distribution of the OH* radiation signal mostly on the overtones of the excitation f_0 frequency. This could find its reason in how the rays are refracted when going through the LOX jet wake as animation analysis suggests. The main frequency component is linked to the wake traslation movement, coincidental with f_0. Higher frequency turbulent structures in the shear-layer result in spatial scattering of the rays which alters their path through the OH rich zones modifying the overall intensity "collected" by the rays. OH rich zones seem to conserve their spatial structure through time. In view of this, it is suggested that refraction of radiation may play a role in the frequency composition of the radiation signal collected by the probe. A quantitative approach by means of a DMD and segregation of both effects (refraction and OH rich layer composition) should be conducted to further asses this phenomenon.

5. Results from the probe analysis, a priori seem to be highly sensitive to the interpolation method inherited, the **"cKD tree"** and inverse distance pondering. This hinders the consistency and mesh independence of the algorithm in place. Future improvements will not demand considerable development as for segregation and single-responsibility principles applied in the development of the new architecture enable fast switch of the method by modifying the *DiscreteField* class. Further studies need to be performed on the influence of the inverse distance exponent p on the signal response.

Bibliography

[1] Wolfgang Armbruster, Justin S. Hardi, Dmitry Suslov, and Michael Oschwald. Injector-driven flame dynamics in a high-pressure multi-element oxygen-hydrogen rocket thrust chamber. *Journal of Propulsion and Power*, 35(3):632–644, 2019.

[2] Scott Kenneth Beinke. *Analysis of Flame Response to Acoustic Forcing in a Rocket Combustor*. PhD thesis, University of Adelaide, Australia, 2017.

[3] Thomas Fiala. *Radiation from High Pressure Hydrogen-Oxygen Flames and its Use in Assessing Rocket Combustion Instability*. PhD thesis, 07 2015.

[4] Stefan GrÃ¶ning, Justin S. Hardi, Dmitry Suslov, and Michael Oschwald. Injector-driven combustion instabilities in a hydrogen/oxygen rocket combustor. *Journal of Propulsion and Power*, 32(3):560–573, 2016.

[5] R. K. Luneburg. *Mathematical Theory of Optics*. University of California Press, 1964.

[6] Johannes Lux and Oskar Haidn. Effect of recess in high-pressure liquid oxygen/methane coaxial injection and combustion. *Journal of Propulsion and Power*, 25(1):24–32, 2009.

[7] Wolfgang Mayer and Hiroshi Tamura. Propellant injection in a liquid oxygen/gaseous hydrogen rocket engine. *Journal of Propulsion and Power*, 12(6):1137–1147, 1996.

[8] Michael F Modest. Chapter 10 - the radiative transfer equation in participating media (rte). In Michael F Modest, editor, *Radiative Heat Transfer (Third Edition)*, pages 279 – 302. Academic Press, Boston, third edition edition, 2013.

[9] Marcus O Conaire, Henry J. Curran, John M. Simmie, William J. Pitz, and Charles K. Westbrook. A comprehensive modeling study of hydrogen oxidation. *International Journal of Chemical Kinetics*, 36(11):603–622, 2004.

[10] Jaka Perovsek. Ray tracing and spectral modeling of excited hydroxyl radiation from cryogenic flames in rocket combustion chambers. Master's thesis, Lulea University of Technology, Department of Computer Science, Electrical and Space Engineering, 2018.

[11] Mikhail N. Polyanskiy. Refractive index database. https://refractiveindex.info. Accessed on 2020-08-21.

[12] Peter J. Schmid. Dynamic mode decomposition of numerical and experimental data. *Journal of Fluid Mechanics*, 656:5–28, 2010.

[13] DI Suslov, J Hardi, B Knapp, and M Oschwald. Optical investigation of the lox-jet disintegration processes at high pressure conditions in a lox/h2 single coaxial injector combustion chamber. *Space Propulsion Conference Paper SP2016*, 3124615, 2016.

[14] Lionel Tesse and Jean-Michel Lamet. Radiative transfer modeling developed at onera for numerical simulations of reactive flows. *AerospaceLab*, 03 2011.

[15] V. Yang and W. E. (eds.) Anderson. *Liquid Rocket Engine Combustion Instability*. AIAA, Washingon, D.C., 1995.

Appendices

A. SMART proposed architecture

The architecture proposed has been sectioned for convenience in four major parts. Altogether, these articulate to yield the behavior of SMART as described in Section 3.1. Though accounting for the requirements fixed in Table 3.1. These are:

1. Data sourcing and preparation
2. Thermochemical library
3. Ray tracing section
    a Rays generation at device level
    b Ray propagation
4. Spectral library

In the following subsections, each of these sections is briefly introduced and explained alongside their corresponding class diagrams. Abstract classes are displayed in blue color. Special care was taken during development for proper documentation of the code via *Python docstrings*.

Overall the resulting code counts with more than 5000 lines with approximately 50% of comments and docstrings.

A. Data sourcing and preparation

The class diagram for this section of the code is shown in Figure A.1.

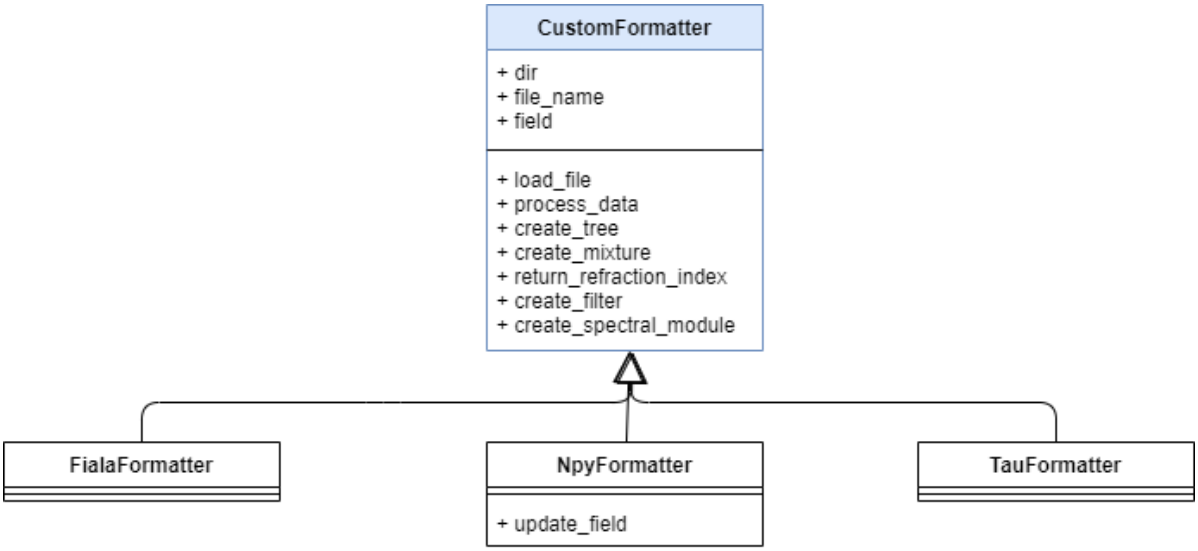

Figure A.1.: **Data sourcing and preparation class diagram.**

Following the diagram, the abstract class *CustomFormatter* is in charge of defining the expected behavior for the data processing module. Each subclass of it (either *FialaFormatter*, *NpyFormatter* or *TauFormatter*) will implement the abstract methods according to the associated data format and eventually return a [numpy] structured array containing the CFD grid and the solution data associated to each point.

As this classes work as an interface between the data files and the actual algorithm, they also command the instantiation of other critical objects such as the *Mixture*, *Filter* and *DiscreteField*[1] objects which serve as source-data repositories.

In such way, requirement *FEAT-1* is fulfilled. To expand the code's capabilities to other CFD solvers, output formats (like *ABVP*) it is only necessary to subclass *CustomFormatter* following the rules of abstract classes inheritance (implement all of the abstract methods respecting input and output arguments, type and significance).

[1] Associated to the refraction index field.

B. Thermochemical library

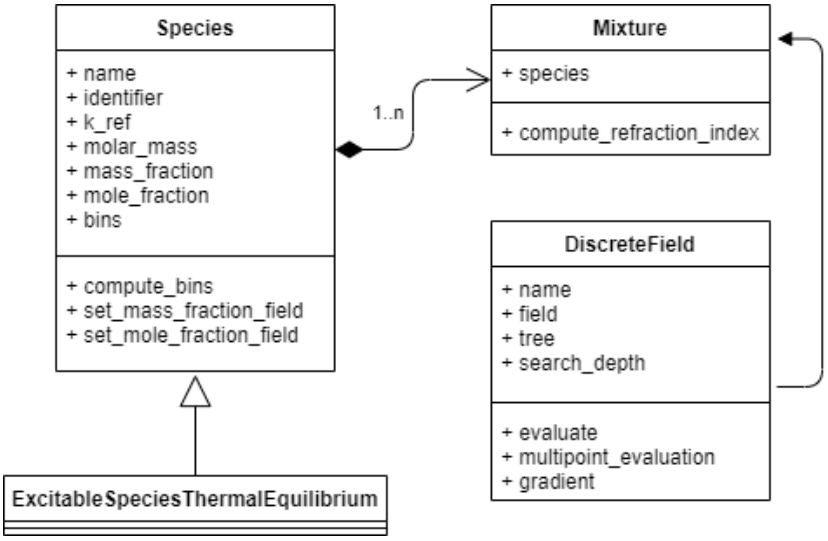

Figure A.2.: **Thermochemical library class diagram.**

The thermochemical library is in place to partially address requirement *MOD-4*. For such, the *Mixture* class is created as a composition of *Species* objects, each one with its own attributes. For instance, following the reduced kinetics scheme from Eqn. (2.10) for hydrogen-oxygen combustion, the mixture is be conformed by the species: $[H_2, O_2, H_2O, H, O, OH]$. Since in particular we are studying the emission of the OH* radical, then for such purpose OH is defined by the *Species'* subclass *ExcitableSpeciesThermalEquilibrium* allocated exclusively to define the excitable nature of this component.

The *Mixture* class has the clear function of collecting the different components and calculating the overall refraction index field by means of Eqn. (2.20). This data is later allocated to a *DiscreteField* instance to be used in the ray-tracing section to feed Eqn. (2.16).

C. Ray tracing section

The ray tracing section is in charge of generating the rays in adequate fashion depending on the optical device used to measure the radiation intensity (camera, optical probe) and later propagate them through space. It must be noticed that propagation from the source (device) till the rays' end-point (combustion domain wall) must include all of the interfaces which may cause a change of its route. Thus, this section proposes a generic approach for modeling refractive interfaces. More details on the mathematical formulation of the method can be found in Appendix B.

C.1. Ray generation at device level

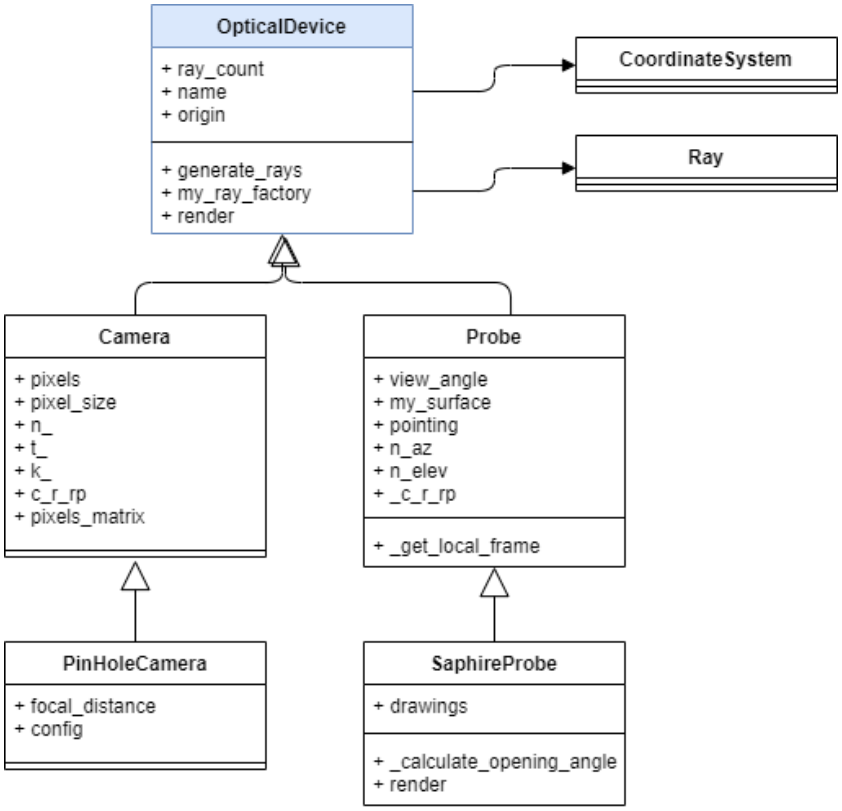

Figure A.3.: **Devices definition class diagram.**

The *OpticalDevice* abstract class has for aims to define the way *Ray* instances are initialized. This involves the definition of a starting point and direction unit vector. Each subclass of optical device (camera, probe) will have its own ray bundle arrangement. For instance, a camera may associate each ray to a pixel with direction normal to the CCD plane, a probe will have a view angle, etc. It must be noted that the *OpticalDevice* is positioned in space according to a *CoordinatesSystem* instance. This class was introduced for convenience to simplify the spatial description of the system. Through this taxonomy, requirement *MOD-2* is satisfied.

C.2. Ray propagation

The class diagram of the ray propagation module is shown on Figure A.4. As it may be observed, there are the already mentioned *Ray*, *CoordinateSystem* and *DiscreteField* classes. Additionally the abstract classes *OpticalDomain*, *OpticalInterface*, *GeometricInterface*, *OpticalVolume*, *ClosedDomain* and *AxisymmetricVolume* help define the hierarchy to achieve requirement *MOD-4* and partially *MOD-1*.

The core idea to achieve the ray propagation lies behind the **"interact"** method between the *OpticalDomain* class and the *Ray* class. By appropriately defining what **"interact"** means, depending of the subclass of *OpticalDomain*, the different behaviors are achieved (polymorphism).

To account for different window geometries, the subclasses of *Geometry* are adapted alongside their associated *Bounds* (class to define specific spatial boundaries). For different combustion chamber geometries the subclasses of *Geometry* and *ClosedDomain*[2] alongside their *Bounds* and _ *TerminationEvents*[3] are adapted.

Finally the *DiscreteField* instance is related to the *DiscretizedVolume* and *AxisymmetricDiscretizedVolume* classes since it's by means of the *DiscreteField* particular instance with the refraction index data that the propagation of the ray is possible with the cloud of points provided from the CFD solution.

Expansion to other window or combustion chamber geometries is achievable by appropriately defining the subclasses of *Geometry* and *ClosedDomain* with the corresponding *Bounds* and _ *TerminationEvents*.

It must be remarked that the *Ray* class behavior was implemented considering a three-dimensional space, thus fulfilling requirement *MOD-5*.

[2] *Python* allows multiple-inheritance, a feature exploited in the present architecture.
[3] *callable* class that triggers the event which finishes the integration of Eqn. 2.16 by indicating the *Runge-Kutta* method that the limit of the domain has been reached.

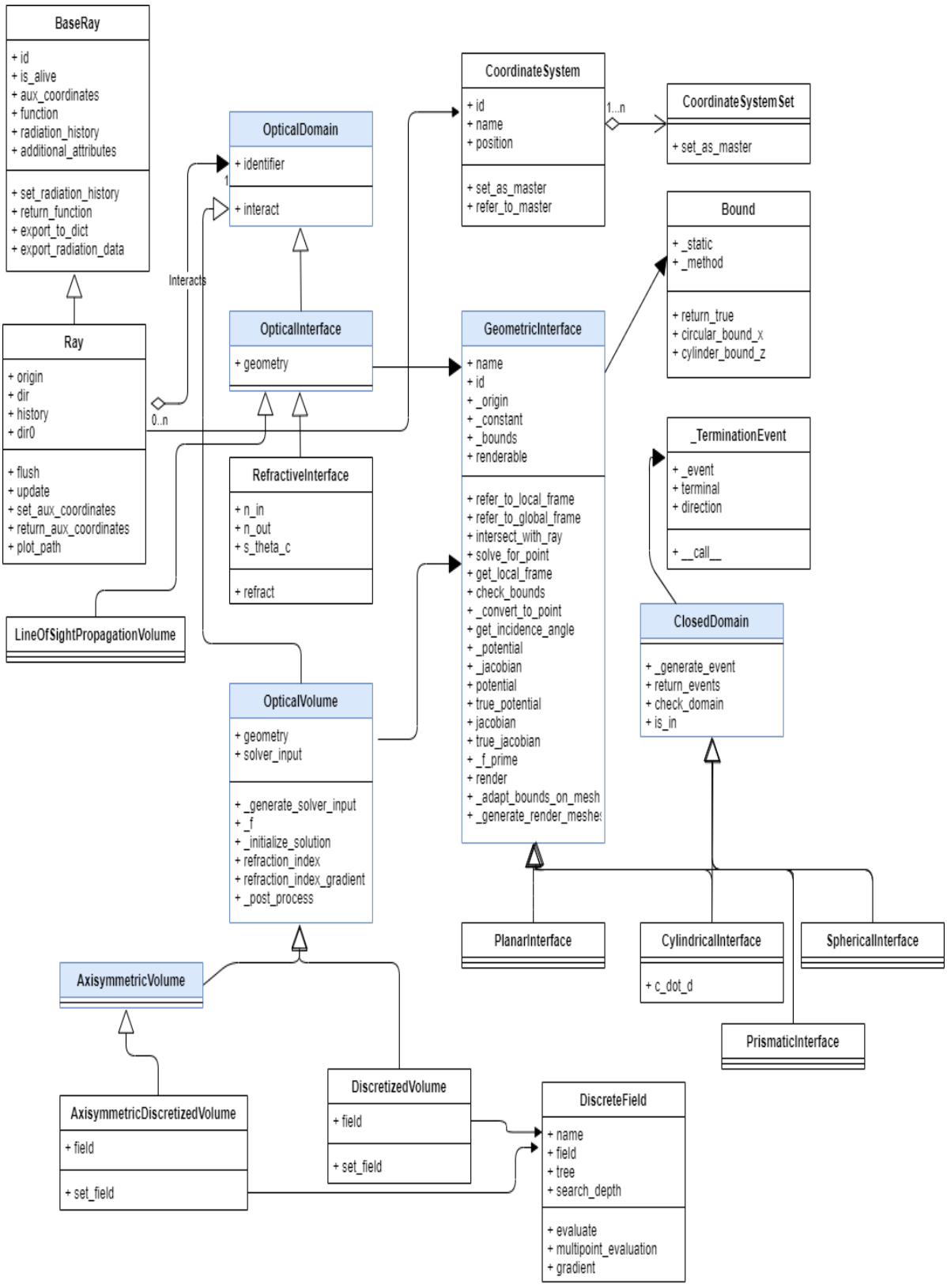

Figure A.4.: **Ray propagation section class diagram.**

D. Spectral library

The *Spectral* library is in charge of solving the spectral radiation intensity through the method explained in Section 2.2.2.3 once the *Ray* instance has already been "propagated" through the combustion domain. Even though not many changes have been put in place in this part of the software with respect to that of Perovsĕk's [10] original SMART code, it has been reframed under the OOP paradigm. The proposed architecture is shown in Figure A.5.

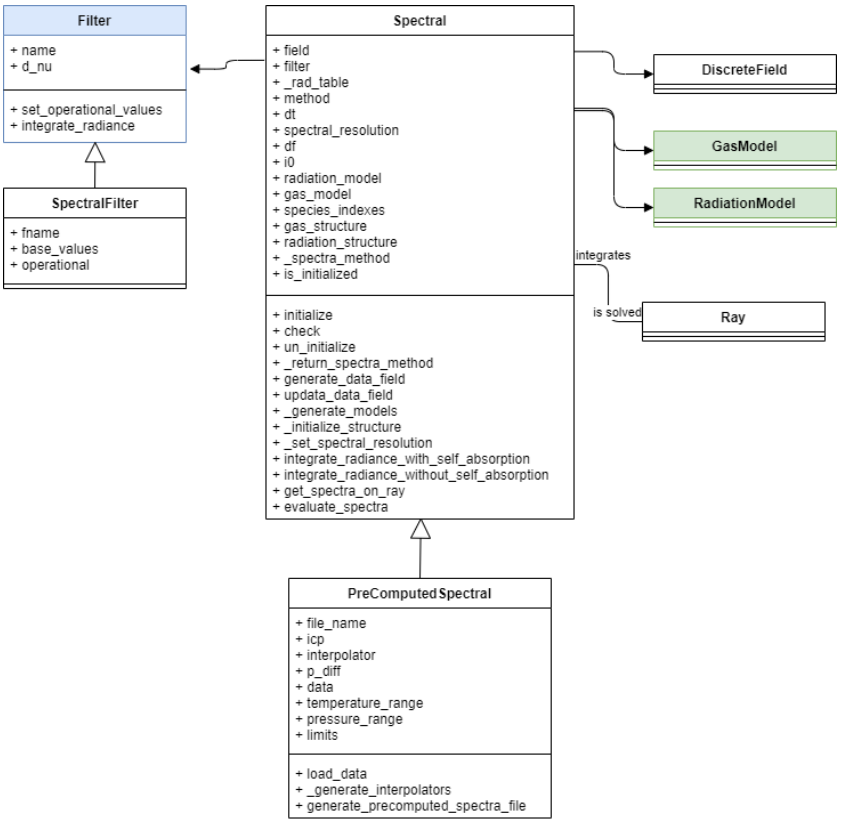

Figure A.5.: **Spectral library class diagram.**

The green classes *GasModel* and *RadiationModel* are both provided by the mentioned *TAU Project Python* wrapped - *C* libraries. A main feature to allow the requirement *PER-1* has been to include the **"initialize"** and **"un_initialize"** methods as part of the *Spectral* class. This is necessary as both *GasModel* and *RadiationModel* are external objects which are not serializable and therefore cannot be mapped to the pool nodes when doing multiprocessing. Thus, the strategy adopted was to instantiate such objects within each process memory instead of in the main program thread. In such way serialization is avoided and the resulting calculation is parallelized.

E. Configuration file

To simplify the traceability of the different cases and ease the setup of the simulation it was decided that all static data concerning the definition of the simulation, that is: geometries, devices, coordinates systems, species, files, etc and their attributes be defined in a single "configuration file" with the *json* format.

A proper class designed to interpret this file name *JsonInterpreter* was created. On each of the relevant classes described above appropriate factory methods were implemented to manage the initialization of the objects in memory with their adequate attributes. By this fashion, migration time from one simulation case of interest to another one was reduced to below a week, fulfilling the requirement *FEAT-2*. This was verified when migrating from *Fiala* cases study to the *HF-9 Rest Probe-C* simulations analysis.

B. Mathematical Modeling of Rays

In the conventional domain of geometry optics, any given ray may be considered as a three dimensional straight line[1] whose direction may be altered by 4 possible phenomenons:

1. Reflection
2. Refraction
3. Diffusion
4. Absorption

In the scope of this appendix only item 2 is modeled, however necessary modifications to account for 1, 3 and 4 do not require intensive further development. It must be noted that these phenomenons constitute interactions between the ray and a given physical media. For piece-wise constant media thus, these phenomena take place at optical interfaces where the domain shows a discontinuity in its optical properties or even a barrier (mirror for item 1).

Therefore, the current ray-tracing model is based in the following *hypotheses*.

H.1 The rays are considered as a straight line when traversing a medium with constant optical properties, namely refraction index (n).

H.2 There exists a *known* potential differentiable function $\phi(\vec{\boldsymbol{r}})$ such that any optical interface (S) the ray may interact with is an equipotential surface given by Eqn. (B.1).

$$S: \ \phi(\vec{\boldsymbol{r}}) - k = 0 \tag{B.1}$$

Where $\vec{\boldsymbol{r}}$ corresponds to the position vector defined in the appropriate coordinate system and k the surfaces potential. Knowing that $\phi(\vec{\boldsymbol{r}})$ is a differentiable scalar-field, then it

[1] Considering a piece-wise constant refraction index (n) field. For more complex fields the assumption of a straight path for the ray is not necessarily true.

can be proved that the normals of S ($\hat{n}(\vec{\boldsymbol{r}})$) are given by Eqn. (B.2)[2]

$$\hat{n}(\vec{\boldsymbol{r}}) = -\frac{\vec{\nabla}\phi(\vec{\boldsymbol{r}})}{\|\vec{\nabla}\phi(\vec{\boldsymbol{r}})\|} \tag{B.2}$$

From **H.1** it is the possible to state that when in a constant medium, a ray may be represented mathematically by Eqn. (B.3).

$$\Gamma : \vec{\boldsymbol{r}} = \vec{\boldsymbol{r}}_{\boldsymbol{0}} + \lambda\hat{\boldsymbol{d}} \tag{B.3}$$

also termed the line parametric equation in which $\vec{\boldsymbol{r}}_{\boldsymbol{0}}$ represents an origin position (ray origin) and $\hat{\boldsymbol{d}}$ its directive vector. For convenience it is stated $\|\hat{\boldsymbol{d}}\| = 1$. λ represents the varying parameter of the line.

Now, it is of interest studying the interaction between the optical surface S and the ray represented by Γ. For such, it is necessary determine, if exists, the intersection point.

A. Ray - Optical Surface Intersection

Even though surface S has already been introduced in Eqn. (B.1) in a general coordinates system, it is normally more convenient to define the potential function with respect to another coordinates system which makes it simpler (frame and origin) to define instead of the global coordinates system. Therefore, the local potential function ($\hat{\phi}$) is introduced such that:

$$\phi(\vec{\boldsymbol{r}}) - k = \hat{\phi}(B_{c\to S}(\vec{\boldsymbol{r}} - \vec{\boldsymbol{r}}_{\boldsymbol{S}})) - k = 0 \tag{B.4}$$

where $B_{c\to S}$ and $\vec{\boldsymbol{r}}_{\boldsymbol{S}}$ are the base change matrix from the global frame to the potential frame (S) and its origin, respectively. Furthermore, replacing Eqn. (B.3) into (B.4) to find the intersection point yields a mono-dimensional root-finding problem.

$$f(\lambda) = \hat{\phi}(B_{c\to S}(\vec{\boldsymbol{r}}_{\boldsymbol{0}} - \vec{\boldsymbol{r}}_{\boldsymbol{S}} + \lambda\hat{\boldsymbol{d}})) - k = 0 \tag{B.5}$$

Depending on the nature of the potential function, the problem may be non-linear. Robust numerical methods, such as *Newton-Raphson's* can be used then to solve the problem. For the

[2] The negative sign indicates the normals are inwards of the surface.

latter, the first-order derivative is required, such that:

$$\frac{df}{d\lambda}(\lambda) = \vec{\nabla}\hat{\phi}(B_{c\to S}(\vec{\boldsymbol{r}}_{\boldsymbol{0}} - \vec{\boldsymbol{r}}_{\boldsymbol{S}} + \lambda\hat{\boldsymbol{d}})) \cdot B_{c\to S}\hat{d} \tag{B.6}$$

Shall a $\lambda_P \in \Re : f(\lambda_P) = 0$ be found, then the intersection point $\vec{\boldsymbol{P}}$ is given by:

$$\vec{\boldsymbol{P}} = \vec{\boldsymbol{r}}_{\boldsymbol{0}} + \lambda_P\hat{\boldsymbol{d}} \tag{B.7}$$

A.1. Intersection Point: Ray-Plane

In the particular case that the optical interface is a plane, then it is possible to access an analytical solution. Let the local potential associated to the plane be defined by:

$$\hat{\phi}(B_{c\to S}(\vec{\boldsymbol{r}} - \vec{\boldsymbol{r}}_{\boldsymbol{S}})) = \hat{\boldsymbol{n}}_{\boldsymbol{p}} \cdot [B_{c\to S}(\vec{\boldsymbol{r}} - \vec{\boldsymbol{r}}_{\boldsymbol{S}})] \tag{B.8}$$

where $\hat{\boldsymbol{n}}_{\boldsymbol{p}}$ is the plane's normal vector. Replacing in Eqn. (B.5) and solving yields,

$$\lambda_P = \frac{k - \hat{\boldsymbol{n}}_{\boldsymbol{p}} \cdot B_{c\to S}(\vec{\boldsymbol{r}}_{\boldsymbol{0}} - \vec{\boldsymbol{r}}_{\boldsymbol{S}})}{\hat{\boldsymbol{n}}_{\boldsymbol{p}} B_{c\to S}\hat{\boldsymbol{d}}} \tag{B.9}$$

The denominator in Eqn. (B.9) imposes the trivial condition that there is no solution to the problem if the ray is orthogonal to the plane normal (the ray is either contained in the plane or never crosses it).

A.2. Intersection Point: Ray-Cylinder

A priori to introducing the solution of the intersection point to a cylinder, the *pseudo-inner product* $\langle , \rangle_D : \mathbb{R}^3 \times \mathbb{R}^3 \to \mathbb{R}$ is presented.

$$\langle \vec{u}, \vec{v} \rangle_D = \vec{u}^T \boldsymbol{D} \vec{v}, \text{ such that } \vec{u}, \vec{v} \in \mathbb{R}^3, \boldsymbol{D} \in \mathbb{R}^{3x3} \tag{B.10}$$

in which $\boldsymbol{D}$ is a symmetric positive semi-definite matrix. As it is proved, the operation fulfills all of the inner-product conditions in $\mathbb{R}^3$ except for positive-definiteness, hence a *pseudo-inner product*.

a **Positive definiteness**:

Let $\vec{u}, \vec{v} \in \mathbb{R}$, then

- Being $\boldsymbol{D}$ positive semi-definite ($\vec{x}^T \boldsymbol{D} \vec{x} \geq 0 \, \forall \, \vec{x} \neq \vec{0} \in \mathbb{R}^3$) $\implies \langle \vec{u}, \vec{u} \rangle_D = \vec{u}^T \boldsymbol{D} \vec{u} \geq 0$.
- If $\vec{u} = \vec{0} \implies \langle \vec{u}, \vec{u} \rangle_D = \vec{0}^T \boldsymbol{D} \vec{0} = \vec{0}$
- Being $\boldsymbol{D}$ not strictly positive definite, then there might $\exists \vec{u} \neq \vec{0} \in \mathbb{R}^3$ such that $\vec{u}^T \boldsymbol{D} \vec{u} = \langle \vec{u}, \vec{u} \rangle_D = 0$, therefore not fully proving the positive-definiteness. Nevertheless, it is possible to define a subspace $V \subset \mathbb{R}^3 \; : \; \vec{0} \in V \wedge \forall \vec{x} \in V \wedge \langle \vec{x}, \vec{x} \rangle_D = 0 \implies \vec{x} = \vec{0}$. Which turns the pseudo-inner product into an inner-product in V.

b **Linearity**:

Let $\vec{u}, \vec{v}, \vec{w} \in \mathbb{R}^3$ and $a, \; b \in \mathbb{R}$, then

- $\langle \vec{w}, a\vec{u} + b\vec{v} \rangle_D = \vec{w}^T \boldsymbol{D} (a\vec{u} + b\vec{v}) = a(\vec{w}^T \boldsymbol{D} \vec{u}) + b(\vec{w}^T \boldsymbol{D} \vec{v}) = a\langle \vec{w}, \vec{u} \rangle_D + b\langle \vec{w}, \vec{v} \rangle_D$
- $\langle a\vec{u} + b\vec{v}, \vec{w} \rangle_D = (a\vec{u} + b\vec{v})^T \boldsymbol{D} \vec{w} = a(\vec{u}^T \boldsymbol{D} \vec{w}) + b(\vec{v}^T \boldsymbol{D} \vec{w}) = a\langle \vec{u}, \vec{w} \rangle_D + b\langle \vec{v}, \vec{w} \rangle_D$

which proves linearity from boths sides.

c **Symmetry** (when in $\mathbb{R}$):

Let $\vec{u}, \vec{v} \in \mathbb{R}$, then

- $\langle \vec{u}, \vec{v} \rangle_D = \vec{u}^T \boldsymbol{D} \vec{v} = (\vec{u}^T \boldsymbol{D} \vec{v})^T = \vec{v}^T \boldsymbol{D}^T \vec{u} = \vec{v}^T \boldsymbol{D} \vec{u} = \langle \vec{v}, \vec{u} \rangle_D$

Therefore, the pseudo-norm is introduced as,

$$\|\vec{u}\|_D = \sqrt{\langle \vec{u}, \vec{u} \rangle_D}, \; \forall \vec{u} \in \mathbb{R}^3$$

It must be noted that due to the lack of positive-definiteness, it can happen that $\exists \vec{u} \in \mathbb{R}^3 : \|\vec{u}\|_D = 0$.

Following this remark, it can be introduced the local potential ($\hat{\phi}$) of the cylinder of radius R (S) by linking it to a local reference frame ($\hat{\boldsymbol{e}}'_{\boldsymbol{i}} : i \in \{1, 2, 3\}$) with the cylinder axis conveniently aligned to one of its axis ($\hat{\boldsymbol{e}}'_{\boldsymbol{3}}$)

$$S : \hat{\phi}(\vec{\boldsymbol{r}}') - R^2 = \|\vec{\boldsymbol{r}}'\|^2 - (\vec{\boldsymbol{r}}' \cdot \hat{\boldsymbol{e}}'_{\boldsymbol{3}})^2 - R^2 = \vec{\boldsymbol{r}}' \cdot (\vec{\boldsymbol{r}}' - x'_3 \hat{\boldsymbol{e}}'_{\boldsymbol{3}}) - R^2 = 0 \tag{B.11}$$

Where $\vec{\boldsymbol{r}}'$ represents a point in local frame coordinates, such that $\vec{\boldsymbol{r}}' = B_{c\to S}(\vec{\boldsymbol{r}} - \vec{\boldsymbol{r}}_{\boldsymbol{0}})$. The term $(\vec{\boldsymbol{r}}' - x_3'\hat{\boldsymbol{e}}_{\boldsymbol{3}}')$ can be interpreted as the vector between any point $\vec{\boldsymbol{r}}' \in S$ and the center of the cross section that contains it. Therefore, it can be replaced by $R\hat{\boldsymbol{n}}'(\vec{\boldsymbol{r}}')$, where $\hat{\boldsymbol{n}}'(\vec{\boldsymbol{r}}')$ corresponds to the normal versor at the point of interest.

Furthermore, it can be stated,

$$\begin{cases} R\hat{\boldsymbol{n}}'(\vec{\boldsymbol{r}}') = \vec{\boldsymbol{r}}' - x_3'\hat{\boldsymbol{e}}_{\boldsymbol{3}}' = M\vec{\boldsymbol{r}}' \\ \text{with } M = \begin{bmatrix} 1 & 0 & 0 \\ 0 & 1 & 0 \\ 0 & 0 & 0 \end{bmatrix} \end{cases} \tag{B.12}$$

Transforming thus to the regular frame of the problem i yields,

$$\begin{cases} S : \phi(\vec{\boldsymbol{r}}) - R^2 = (\vec{\boldsymbol{r}} - \vec{\boldsymbol{r}}_{\boldsymbol{S}})^T \boldsymbol{D}(\vec{\boldsymbol{r}} - \vec{\boldsymbol{r}}_{\boldsymbol{S}}) - R^2 = 0 \\ \text{with } \boldsymbol{D} = B_{c\to S}^T M B_{c\to S} \end{cases} \tag{B.13}$$

Therefore, by looking at $\boldsymbol{D}$ it can be easily concluded that the matrix is symmetric ($\boldsymbol{D} = \boldsymbol{D}^T$) and is positive semi-definite with $Nu(\boldsymbol{D}) \subset \mathbb{R}^3 = \{\vec{x} \in Nu(\boldsymbol{D}) : \ \exists\ \omega \in \mathbb{R},\ \omega\hat{\boldsymbol{e}}_{\boldsymbol{3}}' = B_{c\to S}\vec{x}\}$. Thus, it can be concluded that any element contained in $Nu(\boldsymbol{D})$ will not intersect the cylinder as $Nu(\boldsymbol{D})$ is made by all the vectors parallel to its axis. Thus, it is possible to define a subspace $V \subset \mathbb{R}^3 : Nu(\boldsymbol{D}) \cap V = \vec{0}$ for which the pseudo-product presented before $\langle , \rangle_D : \mathbb{R}^3 \times \mathbb{R}^3 \to \mathbb{R}$ becomes an inner-product ($\langle , \rangle_D : V \times V \to \mathbb{R}$). Thus, rearranging and also replacing Eqn. (B.3) into (B.13) gives,

$$f(\lambda) = \|\vec{\boldsymbol{r}}_{\boldsymbol{0}} - \vec{\boldsymbol{r}}_{\boldsymbol{S}} + \lambda\hat{\boldsymbol{d}}\|_D^2 - R^2 = 0 \tag{B.14}$$

Developing and accommodating terms the quadratic Eqn. (B.15) is obtained.

$$f(\lambda) = \|\hat{\boldsymbol{d}}\|_D^2\lambda^2 + 2\langle\vec{\boldsymbol{r}}_{\boldsymbol{0}} - \vec{\boldsymbol{r}}_{\boldsymbol{S}}, \hat{\boldsymbol{d}}\rangle_D\lambda + (\|\vec{\boldsymbol{r}}_{\boldsymbol{0}} - \vec{\boldsymbol{r}}_{\boldsymbol{S}}\|_D^2 - R^2) = 0 \tag{B.15}$$

Solving for λ yields[3],

$$\begin{cases} \lambda_P = -\alpha \pm \sqrt{\Delta} \\ \text{with } \alpha = \dfrac{\langle \vec{\boldsymbol{r}}_{\boldsymbol{0}} - \vec{\boldsymbol{r}}_{\boldsymbol{S}}, \hat{\boldsymbol{d}} \rangle_D}{\|\hat{\boldsymbol{d}}\|_D^2}, \text{ and } \Delta = \alpha^2 - \dfrac{\|\vec{\boldsymbol{r}}_{\boldsymbol{0}} - \vec{\boldsymbol{r}}_{\boldsymbol{S}}\|_D^2 - R^2}{\|\hat{\boldsymbol{d}}\|_D^2} \end{cases} \tag{B.16}$$

where Δ refers to the discriminant. If $\Delta < 0$, then there is no ray-cylinder intersection, $\Delta = 0$ there's only a tangential intersection and if $\Delta > 0$ then they intersect at two points. Finally, to obtain the intersection point ($\vec{\boldsymbol{P}}$) if corresponds, Eqn. (B.7) must be followed.

A.3. Ray Refraction

Once the intersection point ($\vec{\boldsymbol{P}}$) is identified then it is important to determine the refraction plane and refract the ray. For such purpose the following hypothesis is introduced.

H.3 The ray is refracted and is kept in the refraction plane. The refraction plane normal is given by,

$$\hat{\boldsymbol{n}}_{\boldsymbol{R}} = \frac{\hat{\boldsymbol{d}} \times \hat{\boldsymbol{n}}(\vec{\boldsymbol{P}})}{\|\hat{\boldsymbol{d}} \times \hat{\boldsymbol{n}}(\vec{\boldsymbol{P}})\|} \tag{B.17}$$

where $\hat{\boldsymbol{n}}_{\boldsymbol{R}}$ and $\hat{\boldsymbol{n}}(\vec{\boldsymbol{P}})$ are the refraction plane local optical interface normal at the intersection point, respectively. In case $\hat{\boldsymbol{d}} \parallel \hat{\boldsymbol{n}}(\vec{\boldsymbol{P}})$ then an arbitrary $\hat{\boldsymbol{n}}_{\boldsymbol{R}} \perp \hat{\boldsymbol{n}}(\vec{\boldsymbol{P}})$ is chosen to define the refraction plane. $\hat{\boldsymbol{n}}(\vec{\boldsymbol{P}})$ is determined following Eqn. (B.2).

In addition to the refraction plane normal, it is convenient to define a local frame $F' = (\hat{\boldsymbol{e}}'_{\boldsymbol{1}}, \hat{\boldsymbol{e}}'_{\boldsymbol{2}}, \hat{\boldsymbol{e}}'_{\boldsymbol{3}})$. These are obtained as:

$$\begin{cases} \hat{\boldsymbol{e}}'_{\boldsymbol{2}} = \hat{\boldsymbol{n}}(\vec{\boldsymbol{P}}) \\ \hat{\boldsymbol{e}}'_{\boldsymbol{3}} = \dfrac{\hat{\boldsymbol{d}} \times \hat{\boldsymbol{e}}'_{\boldsymbol{2}}}{\|\hat{\boldsymbol{d}} \times \hat{\boldsymbol{e}}'_{\boldsymbol{2}}\|} \\ \hat{\boldsymbol{e}}'_{\boldsymbol{1}} = \dfrac{\hat{\boldsymbol{e}}'_{\boldsymbol{2}} \times \hat{\boldsymbol{e}}'_{\boldsymbol{3}}}{\|\hat{\boldsymbol{e}}'_{\boldsymbol{2}} \times \hat{\boldsymbol{e}}'_{\boldsymbol{3}}\|} \end{cases} \tag{B.18}$$

[3] It must be noted that the problem yields no solution when $\|\hat{\boldsymbol{d}}\|_D = 0$. This is coherent with the fact that if the ray is parallel to the cylinder axis then $\lambda_P \to \infty$, which means they never meet. Thus, in order to have a solution it must be enforced too that $\hat{\boldsymbol{d}} \in V$.

This yields a base change matrix from the global canonical frame ($\hat{\boldsymbol{e}}_{\boldsymbol{i}} : i \in \{1, 2, 3\}$) of the form $[B_{c\to F}]_{ij} = \hat{\boldsymbol{e}}'_{\boldsymbol{i}} \cdot \hat{\boldsymbol{e}}_{\boldsymbol{j}}$.

With this, it is now possible to perform the refraction of the ray by means of *Snell's law* (B.19).

$$n_{in} \sin\theta_{in} = n_{out} \sin\theta_{out} \rightarrow \sin\theta_{out} = \frac{n_{in}}{n_{out}} \sin\theta_{in} \tag{B.19}$$

in which $\theta_{in},\ \theta_{out}$ are the incidence and refracted angles and n_{in}, n_{out} the refraction indexes of the media involved, respectively. The incidence angle is determined by Eqn. (B.20). It must be noted that $\theta_{in} \in (-\frac{\pi}{2}, \frac{\pi}{2})$.

$$\cos\theta_{in} = \hat{\boldsymbol{d}} \cdot \hat{\boldsymbol{e}}'_{\boldsymbol{2}},\ \sin\theta_{in} = \hat{\boldsymbol{d}} \cdot \hat{\boldsymbol{e}}'_{\boldsymbol{1}} \tag{B.20}$$

Thus, the refracted ray director ($\hat{\boldsymbol{d}}_{\boldsymbol{r}}$) in local frame coordinates is thus[4]: $\hat{\boldsymbol{d}}'_{\boldsymbol{r}} = [\sin\theta_{out},\ \cos\theta_{out},\ 0]^T$. Therefore in global frame the new director is given by Eqn. (B.21).

$$\hat{\boldsymbol{d}}_{\boldsymbol{r}} = B^T_{c\to F} \hat{\boldsymbol{d}}'_{\boldsymbol{r}} \tag{B.21}$$

Finally, the resulting refracted ray (Γ_r) Eqn. is given by (B.22).

$$\Gamma_r : \vec{\boldsymbol{r}} = \vec{\boldsymbol{P}} + \lambda \hat{\boldsymbol{d}}_{\boldsymbol{r}} \tag{B.22}$$

The previously discussed algorithm has been implemented in a *Python* object-oriented program. An example of its results are shown in Figure B.1.

[4] $\cos\theta_{out} = \sqrt{1 - \sin^2(\theta_{out})}$

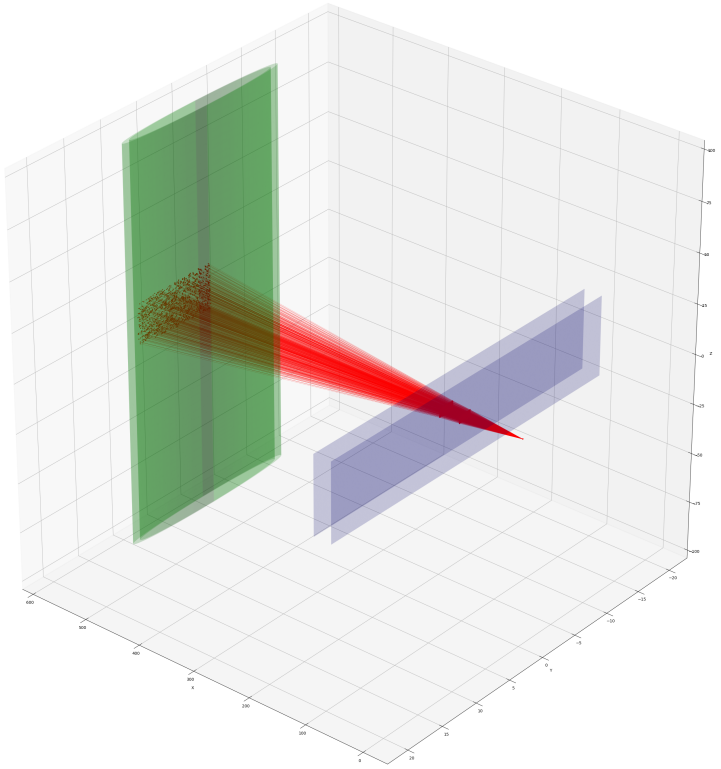

Figure B.1.: **Preliminary results from parametric ray modelling refraction.**

C. Configuration Files of studied cases

A. Configuration file setup, Fiala case

The configuration file mentioned in Section E of Appendix A was adapted to account for the experimental setup used by Fiala and also to replicate as much as possible the ray tracing conditions defined in his thesis for the simulation of radiation. In the file, the initialization data required for the classes which form the codes architecture is provided. The objects as described by the file are shown in Tables C.1 through C.4.

The way to interpret the objects is that every ray generated by the camera (one ray per pixel) will **"interact"** with each of the *OpticalDomain* subclasses listed in Table C.3 according to the order provided by its "Identifier" attribute. For a *RefractiveInterface* this means the ray will be refracted at the intersection point between the geometry associated and the ray projected path. For the *AxisymmetricDiscretizedVolume*, the **"interact"** dynamics, and instead of a simple refraction, the ray is propagated through the volume following the *Eikonal* equation and the refraction index field. After each **"interact"** call, the ray object attributes, namely origin point and direction vector are updated.

The resulting propagated rays and the geometric arrangement are better displayed in Figure 4.5. The representation has been generated through the **"render"** and **"plot_path"** methods from the *Geometry* and *Ray* classes, respectively.

Table C.1.: **Coordinates System used to define objects origins. The master (system to which all is referred to) is chosen as the "CC System".**

Identifier	Class	Name
0	*CoordinateSystem*	CC System
1	*CoordinateSystem*	Camera Sys

Table C.2.: ***Geometries*** **defined.**

Identifier	Class	Name	Origin
0	*PlanarInterface*	Front Window Quartz	CC System
1	*PlanarInterface*	Back Window Quartz	CC System
2	*CylindricalInterface*	CC - Out	CC System
3	*CylindricalInterface*	CC - In	CC System

Table C.3.: ***OpticalDomain*** **instances implemented to replicate Fiala case.**

Identifier	Class	Associated Geometry
0	*RefractiveInterface*	Front Window Quartz
1	*RefractiveInterface*	Back Window Quartz
2	*RefractiveInterface*	CC - Out
3	*RefractiveInterface*	CC - In
4	*AxisymmetricDiscretizedVolume*	CC - In

Table C.4.: ***OpticalDevice*** **table.**

Name	Class	Origin	Pixels
CAM-1	*PinHoleCamera*	Camera Sys	80×20

B. Configuration file setup, HF-9 REST case

In similar fashion to what was explained in Section A if this Appendix, for the probe modeling the objects defined in the configuration file, following the architecture explained in Section A are listed in Tables C.5 through C.8. *OpticalDomain* 0 is used as a dummy interface to perform the intersection of the rays since they originate from the cone vertex of the probe mentioned in the previous section, reach the thrust chamber diameter and then the CFD domain boundary defined around the axis of injector 10.

Table C.5.: **Coordinates System used to define objects origins. The master (system to which all is referred to) is chosen as the "Injector-10".**

Identifier	Class	Name
0	*CoordinateSystem*	CC System
1	*CoordinateSystem*	Injector-10
2	*CoordinateSystem*	Probe C Sys

Table C.6.: ***Geometries*** **defined, HF-9 REST case.**

Identifier	Class	Name	Origin
0	*CylindricalInterface*	BKD-In-Surface	CC System
1	*CylindricalInterface*	CFD-Domain Boundary Injector 10	Injector-10

Table C.7.: ***OpticalDomain*** **instances implemented for HF-9 REST case.**

Identifier	Class	Associated Geometry
0	*RefractiveInterface*	CFD-Domain Boundary Injector 10
1	*DiscretizedVolume*	CFD-Domain Boundary Injector 10

Table C.8.: ***OpticalDevice*** **table, HF-9 REST case.**

Name	Class	Origin	Rays #
PRB-C	*SaphireProbe*	Probe C Sys	100

D. Ray Tracing Validation

Following the approach outlined by Perovsĕk in his thesis [10], the same benchmark-case for the ray tracing section of the new SMART implementation was considered. That is the one of the *Luneburg* lens [5]. Here, rays are propagated within a sphere with refraction index defined by Eqn. (D.1), where n_0 is a constant and r is the distance to the sphere's center. Considering parallel incidence of the rays, it is known that these converge to a single point on the opposite side of the sphere.

The numerical solution given by the implicit integration of the *Eikonal* equation (2.16) by means of a *Runge-Kutta* method confirms this effect, as it is observed in Figure D.1. All the parallel incident rays simulated converge to a unique point as expected.

$$n(r) = n_0\sqrt{2 - r^2} \tag{D.1}$$

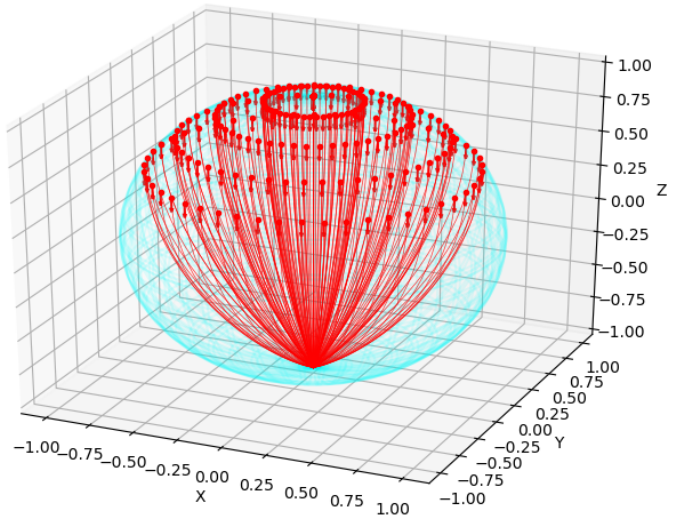

Figure D.1.: ***Luneburg* lens simulation. Parallel rays incidence.**

E. Fiala cases - additional images

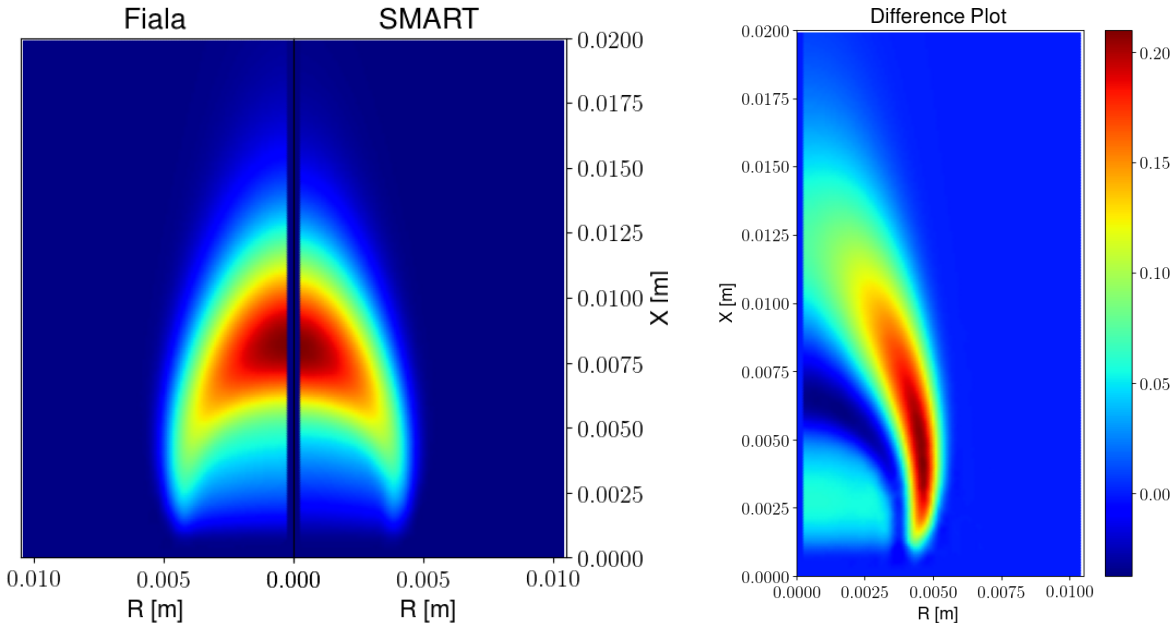

(a) **Comparison of normalized OH^* radiation intensity, Fiala SM-SMART tool.**

(b) **Difference, normalized OH^* radiation intensity.**

Figure E.1.: **Results *LBSSR03-40-10.00* case.**

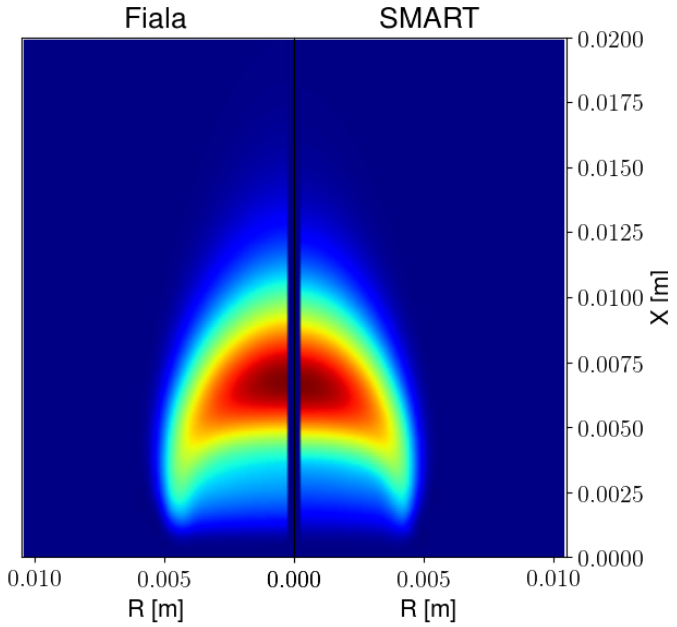

(a) Comparison of normalized OH^* radiation intensity, Fiala SM-SMART tool.

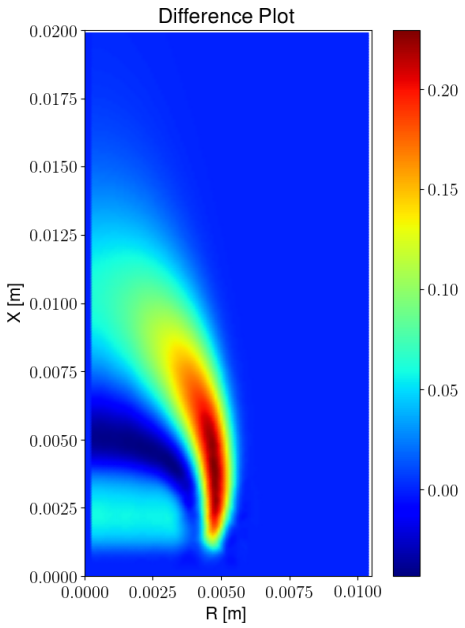

(b) Difference, normalized OH^* radiation intensity.

Figure E.2.: Results ***LBSSR03-40-20.00*** case.

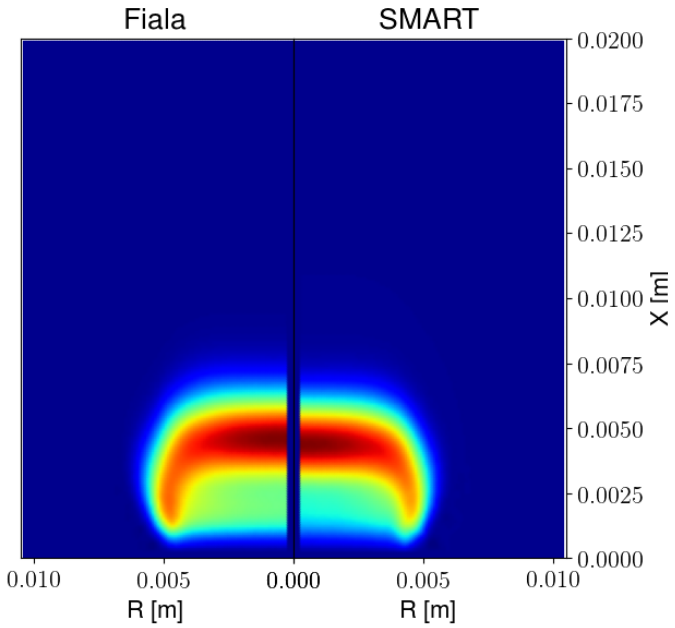

(a) Comparison of normalized OH^* radiation intensity, Fiala SM-SMART tool.

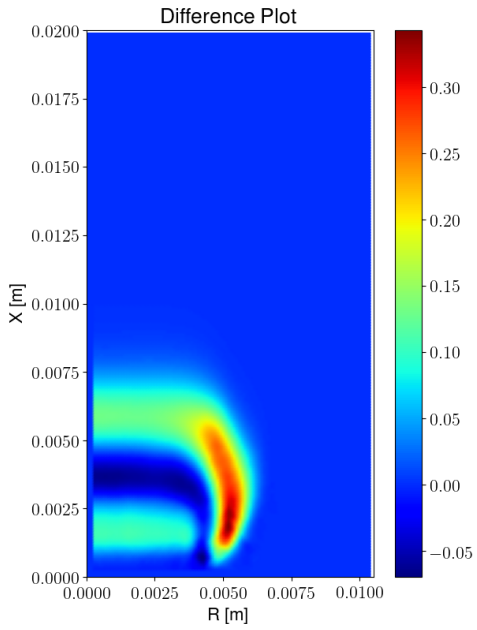

(b) Difference, normalized OH^* radiation intensity.

Figure E.3.: Results ***LBSSR03-40-40.00*** case.